Contents lists available at ScienceDirect

Acta Materialia

journal homepage: www.elsevier.com/locate/actamat



Full length article

Synergetic effects of solute and strain in biocompatible Zn-based and Mg-based alloys



Y.Q. Guo^{a,b,1}, S.H. Zhang^{a,b,1}, I.J. Beyerlein^c, D. Legut^d, S.L. Shang^e, Z.K. Liu^e, R.F. Zhang^{a,b,*}

- ^a School of Materials Science and Engineering, Beihang University, Beijing 100191, PR China
- b Center for Integrated Computational Materials Engineering (International Research Institute for Multidisciplinary Science) and Key Laboratory of High-Temperature Structural Materials & Coatings Technology (Ministry of Industry and Information Technology), Beihang University, Beijing 100191, PR China
- ^c Department of Mechanical Engineering, Materials Department, University of California at Santa Barbara, Santa Barbara, CA 93106, USA
- ^d IT4Innovations Center, VSB-Technical University of Ostrava, CZ-70833 Ostrava, Czechia
- e Department of Materials Science and Engineering, The Pennsylvania State University, University Park, PA 16802, USA

ARTICLE INFO

Article history: Received 6 June 2019 Revised 16 August 2019 Accepted 30 September 2019 Available online 4 October 2019

Keywords: Zinc alloy Strain effect Stacking fault energy Dislocation core structure Peierls stress

ABSTRACT

Zn-based and Mg-based alloys have been considered highly promising biodegradable materials for cardiovascular stent applications due to their excellent biocompatibility and moderate in vitro degradation rates. However, their strength is too poor for use in cardiovascular stents. The strength of these metals can be related to the sizes of the dislocation cores and the threshold stresses needed to activate slip, i.e., the Peierls stress. Using density functional theory (DFT) and an ab initio-informed semi-discrete Peierls-Nabarro model, we investigate the coupled effect of the solute element and mechanical straining on the stacking fault energy, basal dislocation core structures and Peierls stresses in both Zn-based and Mgbased alloys. We consider several biocompatible solute elements, Li, Al, Mn, Fe, Cu, Mg and Zn, in the same atomic concentrations. The combined analysis here suggests some elements, like Fe, can potentially enhance strength in both Zn-based and Mg-based alloys, while other elements, like Li, can lead to opposing effects in Zn and Mg. We show that the effect of solute strengthening and longitudinal straining on SFEs is much stronger for the Zn-based alloys than for the Mg-based alloys. DFT investigations on electronic structure and bond lengths reveal a coupled chemical-mechanical effect of solute and strain on electronic polarization, charge transfer, and bonding strength, which can explain the weak mechanical effect on Zn-based alloys and the variable strengthening effect among these solutes. These findings can provide critical information needed in solute selection in Zn-based and Mg-based alloy design for biomedical applications.

© 2019 Acta Materialia Inc. Published by Elsevier Ltd. All rights reserved.

1. Introduction

Advanced metal-based biodegradable materials, such as Mg-based, Zn-based and Fe-based alloys, are currently being studied for potential use in several biomedical applications, such as cardiovascular stents and in bone fixation, due to their excellent biocompatibility [1–4], promising in-vitro biodegradability [5–7] and sufficient mechanical support [8,9]. The more commonly used Ti-based alloys for biomedical applications, while being biocompatible, are not biodegradable [10]. Among the biodegradable candidates, Mg-based alloys have generally been considered the

most promising due to their lightweightness, and similar stiffness to natural bone [11,12]. However, broad applications of these alloys have been limited by their fast degradation rate (-2.37 V vs. Standard Hydrogen Electrode (SHE)) [5] and insufficient mechanical strengths for mechanical support in implantation. Zn-based alloys, on the other hand, have been recently found to possess much lower degradation rates (-0.8 V vs. SHE) [5] in the human body than Mg-based alloys. Nevertheless, the ultimate tensile strength (UTS) of pure Zn in the as-cast condition is only 20 MPa and its elongation to failure (EL) is 0.3% [13], both much lower than the corresponding benchmark yield strength > 200 MPa, UTS > 300 MPa and EL > 15-18% values required for cardiovascular stents [2,6,14]. The low strengths of Mg and Zn can in part be attributed to their hexagonal close packed (hcp) crystal structure, which easily facilitates slip in one direction but highly constrains it in other directions, an anisotropy that can lead to localization and

 $^{^{}st}$ Corresponding author at: School of Materials Science and Engineering, Beihang University, Beijing 100191, PR China.

E-mail address: zrf@buaa.edu.cn (R.F. Zhang).

 $^{^{1}}$ These authors contributed equally.

brittle fracture during deformation. The last candidate material, Fe-based alloys, has a body-center cubic structure, and does not bear such problems and possesses sufficient mechanical strength and low degradation rates ($-0.440\,\mathrm{V}$ vs. SHE) [5,15,16]. However, their application is generally hindered by their rapid accumulation of degradation products onto vessel walls [2,17]. With mechanical strength as major concerns for the more promising candidate Mg-based and Zn-based alloys, intense efforts have focused on improving or modifying their mechanical properties.

For Mg-based and Zn-based alloys, some works have shown that appropriate selection of alloying elements can lead to strengthening as well as enhancements in ductility, (i.e., referred to as "ductilizing"). Jiang et al. [18] reported that the mechanical properties of Mg-based alloy can generally be improved, achieving a UTS of 310 MPa and an elongation of 26%. As-prepared Mg-Zn-Ca-Mn alloys have attained even higher elongations up to 30% and a high compression/tensile yield ratio \sim 0.8 [19]. By first-principles calculations, Shang et al. [20] suggest that the increased equilibrium volume that accompanies the addition of some solutes in Mg can reduce the intrinsic stacking fault energies (SFE) and ideal shear strengths. Using similar methods, Buey et al. [21] and Yin et al. [22] proposed that solutes would modify the stacking fault energy in such a way that the hard-to-activate pyramidal $\langle c+a \rangle$ dislocations could be activated.

In comparison with Mg-based alloys, much less experimental and theoretical investigations into solute effects in Zn-based alloys have been performed, since it was only recently in 2013 that an experimental study [14] reported that Zn had great potential as a biodegradable material. Soon after biodegradable Zn-based alloys, containing Mg, Al, Cu, Li, Sr, Mn, and/or Ca as solute elements, have demonstrated vastly improved mechanical properties [23–40]. In Ref. [29], the yield strength, tensile strength and elongation of Zn-0.8Mg reached 203 MPa, 301 MPa and 15%, respectively. For Zn-1Mg-0.1Mn and Zn-1Mg-0.1Sr alloys, a yield strength, tensile strength and elongation of 195 MPa, 300 MPa and 22% or above was reported [31]. With addition of Cu, the yield strength, tensile strength, and elongation of the Zn-4Cu alloy reached impressive levels of 250 MPa, 270 MPa, and 51%, respectively [32].

Many of these structural properties are slightly lower than Mg alloys, for similar alloying elements, e.g., the Mg–Zn–Ca–Mn systems [19]. For some of these solutes, like Cu, improvements seen in Zn-alloys have not been reported in Mg-alloys. The individual effects of the same solutes on dislocation motion in Mg alloys and Zn alloys certainly deserves further attention.

Apart from solute strengthening of Mg-based and Zn-based alloys, the additional effects of strain and hydrostatic stress on the solute strengthening should be taken into consideration since such mechanical fields can modify the SFE, dislocations core structure, and Peierls stress. The biodegradable materials of interest here, when used in human-body implant applications, do experience pressure or multiaxial strain conditions, e.g., vessel shrinkage, pulsatile pressure, etc. [41,42]. Some of the processing procedures used in order to prepare these materials for manufacturing parts involve combinations of high pressures and straining, e.g., extrusion, rolling, forging, etc. [19,43–45]. In addition to the experimental work, recent computational investigations have also reported a profound strain effect on the strengthening and "ductilizing" of Mg-based and Zn-based alloys. For instance, a recent DFT study [46] revealed an effect of volumetric strain on the SFE and dislocation core structure of Mg-based alloys. It was found that the variations of these critical parameters controlling strength under strain can be attributed to the strain-induced electronic polarization and redistribution of valence charge density at hollow sites. Also using DFT methods, a similar pressure effect on plasticity was reported by Liu et al. [47] for the newly developed Zn-based alloys, showing that the twin formation energies of Zn–Al alloys can be modified significantly by external pressure.

In general, the effect of external stress on the effectiveness of solute strengthening in Mg-based and Zn-based alloys are not additive, since the strain and pressure can potentially change the c/a ratio and modify SFEs on the basal plane. Such changes can augment the core structures of the dislocations, and consequently their mobility and Peierls stress. In Ref. [48], it was proposed that hydrostatic pressure might help to activate different slip systems in the AZ31 alloy, and some experimental observations providing support were given for the Mg-based alloy. Further, for hcp metals like Zn and Mg, the c/a ratio can be correlated with the types of plastic deformation modes that are activated [49]. Hcp metals like Mg, Re, Zr and Ti with c/a ratios less than 1.63 often have a good plasticity and can deform via multiple twin modes, available either under tensile or under compressive loading, while for hcp metals like Zn, with larger c/a ratios than 1.63, twinning can be activated under compression, and poor plasticity when subjected to tensile load is exhibited. Since both strains and solutes can affect the cores of dislocations and hence the stresses required to move them, it is possible that solute may take on a different role when the crystal is subject to an applied pressure or axial strains.

In the present work, we employ a combination of ab initio and Peierls-Nabarro dislocation calculations to investigate the effect of several biocompatible alloying elements on the SFE, dislocation core structures and Peierls stress for basal dislocations in Zn-based and Mg-based alloys and changes in these effects under strain. To facilitate this comparison, we consider the same alloying elements in the same atomic concentration for both Zn-based and Mg-based alloys. The focus on basal dislocation motion is motivated by their dominance during the plastic deformation of Mg-based and Zn-based alloys. In what follows, the computational methods are introduced in Section 2 and the results are presented in Section 3, including the influence of the solutes on dislocation properties under zero stress and also under hydrostatic pressures or longitudinal straining. We show, for instance, that solutes Fe and Mn can improve mechanical strength for both Zn and Mg, while Li influences the properties of Zn and Mg dislocations in opposing ways. Zn and Mg alloys can also exhibit distinct responses to hydrostatic pressure and longitudinal strain. To explain the observed individual effects on Zn vs. Mg alloys, we calculate the variations of bond length and their electronic structure with solute and straining. In Section 4, we discuss an apparent synergetic influence of solute additions and straining that is revealed from the analysis. In particular, the electronic structure calculations reveal a distinct electronic polarization and charge transfer that can be linked to the coupled effect of solute and strain on dislocation properties. These findings can benefit alloy design of Zn-based and Mg-based alloys for improved mechanical strength, and their use as viable biodegradable cardiovascular stent materials.

2. Computational approaches

2.1. First-principles calculation

First-principles calculations in this work are performed using the Vienna *ab initio* simulation package (VASP) [50] with the projector augmented wave (PAW) method [51]. The Perdew-Burke–Ernzerhof (PBE) version [52] of the Generalized Gradient Approximation (GGA) is adopted for the exchange-correlation approximation. We selected a plane-wave cutoff energy of 600 eV and $13 \times 15 \times 3$ Γ -centered k-point meshes after careful tests to ensure convergence (as evident in Fig. S1 in the Supplementary material). The energy convergence criterion of the electronic self-consistency is set at 10^{-6} eV/cell, and all forces acting on atoms are lower than the force convergence criterion 0.05 eV/Å in ionic

relaxation. DFT calculations under high pressure are enabled by activating the parameter "PSTRESS" in VASP and allowing only the atomic positions to relax. For the electronic self-consistency calculation, we used the Methfessel–Paxton (MP) method [53] with a smearing width of 0.01 eV. As validation of these first-principles results, we compared the calculated lattice parameters and elastic properties of pure Zn and pure Mg with the previous values [46,54–65]. Tables S1 and S2 in the Supplementary material present these results, showing a good agreement.

2.2. Stacking fault energy

The stacking fault energy surface or γ -surface, on the slip plane, was first defined by Vitek [66], as the excess energy associated with the shearing of two adjacent planes along a particular slip direction. The stacking fault energy γ_{SF} can be determined via:

$$\gamma_{SF} = \frac{1}{\Lambda} (E_{SF} - E_{Bulk}), \tag{1}$$

where E_{SF} and E_{Bulk} are the energies of the structure with and without stacking fault, respectively, and A is the area of stacking fault.

In this work, we aim to determine the effect of solute types for the situation in which solute concentrations are dilute and separated, below the solubillimit. Due to computational size limitations, supercell size selected is such that in all solute cases here, the areal solute concentration on the basal plane fault is 25% and the global concentration is 2%. Consequently, for most cases, however, these concentrations could exceed the solubility limit, and with such concentrations in actuality, precipitates could form. First, relatively higher concentrations in the fault is possible. According to Suzuki effect [67], the solutes will prefer to segregate in the faulted region. Also, it is important to bear in mind that the solubility may be modified by different preparation conditions, such as those involving pressures or mechanical straining [47,68]. Nonetheless, to ensure our calculations at these concentrations (2% in bulk) would provide adequate representation for lower concentrations below the solubility limit (1% in bulk). We repeated SFE energy calculations with larger supercell sizes wherein the concentrations were lower. Fig. S2 in the supplement demonstrates that the calculated stacking fault energies do not change appreciably (and converge in some cases) with larger supercell sizes and lower concentrations. This test indicates that results for 2% would apply to those at much lower solute concentration below the solubility limit.

Fig. 1a shows the atomic structure of the plane in the perfect lattice structure (...ABABAB...), and the I_2 stacking fault (...ABABCACA...). To create the model of the alloyed plane, an atom within one faulted plane (0001) is replaced by one solute atom X. Fig. 1b presents the projected (0001) plane, and Fig. 1c depicts the slip path within the γ -surface to form the I_2 stacking fault.

To calculate the γ -surface, two distinct methods were at first considered. One method is called alias shear [69], which involves displacing to the periodic cell in shear direction with changing the cell vectors at the same time. The second method is slab shear [70], which changes the atomic positions but preserves the cell shape. Fig. 1d compares the SFE profile for the basal plane of Zn and Mg from these two approaches. Minor differences are observed (when convergence is obtained). On this basis, the alias shear method is used in the calculations that follow.

During the calculation for the stacking fault energy, two kinds of relaxation methods: (i) the rigid mode and (ii) the relaxed mode, were at first tried and compared. The former fixes all atomic positions inside the two sheared blocks during the relaxation step, while the latter allows the atomic positions to move perpendicular

to the fault plane. For both Mg-based and Zn-based alloys, these two methods generate γ_{I2} and γ_{UI2} with some difference, (see Table S3 in the Supplementary material), showing an effect of relaxation process on the calculated γ_{SF} [71]. In the present study, we used consistently the second relaxation scheme.

2.3. Dislocation core structure and Peierls stress

In general, dislocation cores can be too large to be modeled directly by DFT, and therefore, alternative methods need to be employed. To date, three methodologies have been used to calculate the dislocation core structures from quantities calculated from first principles: (1) a solution based on flexible boundary conditions [72–74]; (2) an solution employing the concept of a dislocation dipole array [75,76]; and (3) the semi-discrete variational Peierls–Nabarro (P-N) model by Bulatov and Kaxiras [77] and Lu [78]. In this study, we used the third method to approximate the core structure and obtain an estimate of the Peierls stress for a pure edge basal dislocation.

In all cases, we consider a basal edge dislocation lying in the x-z plane with its line sense directed along the z-axis ([1 $\bar{1}$ 00]) and its Burgers vector of $\vec{b} = 1/3[\bar{1}\bar{1}20]$ directed along the x-axis.

In this model, the total energy of the dislocation E_{tot} includes misfit energy E_{misfit} and elastic energy E_{el} [77]:

$$E_{tot} = \sum_{i} \gamma (u_x(x_i), u_z(x_i)) \cdot \Delta x + K_e \cdot \sum_{ij} \chi_{ij} \rho_{x,i} \rho_{x,j}$$

$$+ K_s \cdot \sum_{ij} \chi_{ij} \rho_{z,i} \rho_{z,j},$$
(2)

where the first term in Eq. (2) is the misfit energy expressed as:

$$E_{misfit}(\mu) = \sum_{m} \gamma (u_x(m\Delta x - \mu), u_z(m\Delta x - \mu)) \cdot \Delta x, \tag{3}$$

where $m = 0, \pm 1, \pm 2, \pm 3,... \pm \infty$, and the second and third terms in Eq. (2) are the elastic energy given by:

$$\rho_{x,i} = (u_{x,i} - u_{x,i-1})/(x_i - x_{i-1}), \ \rho_{z,i} = (u_{z,i} - u_{z,i-1})/(x_i - x_{i-1}),$$
(4a)

$$\chi_{ij} = 3/2 \cdot \varphi_{i,i-1} \varphi_{j,j-1} + \psi_{i-1,j-1} + \psi_{i,j} - \psi_{i-1,j} - \psi_{i,j-1}, \tag{4b}$$

$$\psi_{i,j} = 1/2 \cdot \varphi_{i,j}^2 \ln |\varphi_{i,j}|, \ \varphi_{i,j} = x_i - x_j,$$
 (4c)

and the energy factor

$$K_e = G/(4\pi (1 - \nu)), K_s = G/(4\pi),$$
 (4d)

where x_i are the reference positions, Δx is defined as the shorest distance between two equivalent atomic rows along the dislocation line direction as the absence of a dislocation, G is the effective shear modulus and ν is the effective Poisson's ratio. To facilitate comparisons across different cases of the solutes and applied strain states, we use the same set of elastic constants, i.e., $K_e = 4.35 \, \text{GPa}$ and $K_S = 3.25 \, \text{GPa}$ for all Zn-based alloys, and $K_g = 2.38 \, \text{GPa}$ and $K_S = 1.72 \, \text{GPa}$ for all Mg-based alloys.

As proposed in Ref. [79], the disregistry in the x and z directions, $u_x(x)$ and $u_z(x)$, for this dislocation can be well represented by equation below

$$u_{x}(x) = \frac{b}{2\pi} \left(\arctan \frac{x - d_{x}/2}{w_{x}} + \arctan \frac{x + d_{x}/2}{w_{x}} \right) + \frac{b}{2}$$

$$u_{z}(x) = \frac{\sqrt{3}b}{6\pi} \left(\arctan \frac{x - d_{z}/2}{w_{z}} - \arctan \frac{x + d_{z}/2}{w_{z}} \right),$$
(5)

where d_X (or d_Z) is the separation between edge (or screw) components of the two partial dislocations ("split distance" for short).

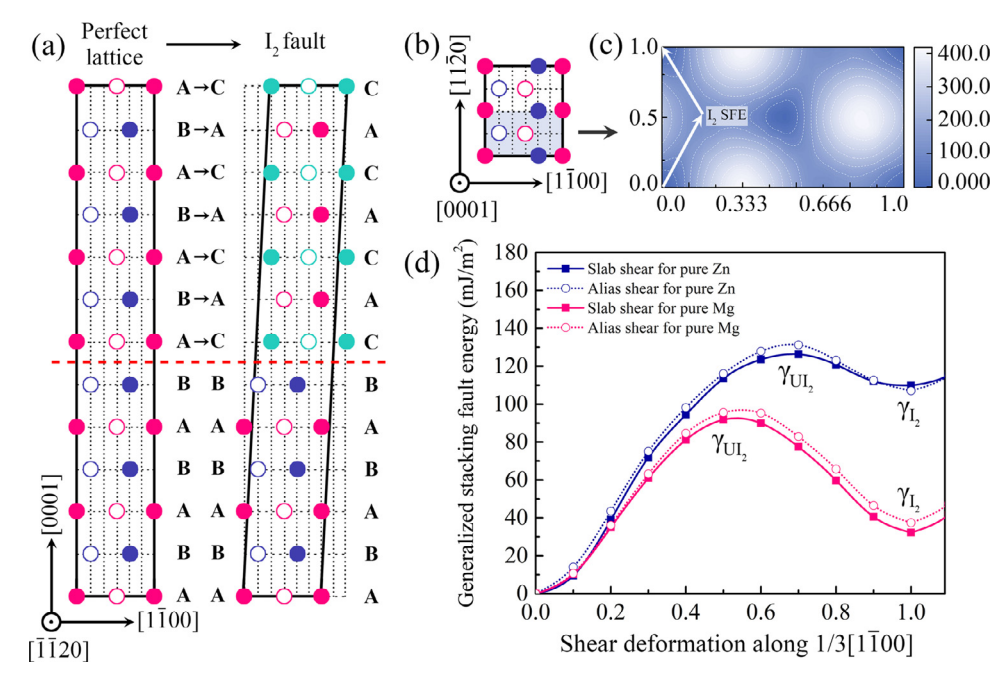


Fig. 1. (a) Schematic illustrations of the perfect lattice and the basal stacking fault, configurations generated via the alias shear. The letters A, B and C represent different stacking sequences of the (0001) planes, which are identified by pink, blue and cyan symbols, respectively. The solid and open circles represent the atomic coordinates at 0 and ½ along [$\bar{1}\bar{1}20$] direction, respectively; and the dotted line indicates the stacking fault position. The movements of different (0001) planes along the [$\bar{1}\bar{1}00$] direction during the alias shear deformation are shown by the arrows (\rightarrow), while the atoms without arrows (\rightarrow) remain in their original positions during the alias shear deformation. (b) Schematic description of the directions in the (0001) plane, the colored area is the shear region. (c) Full γ-surface of pure Zn of the basal (0001) plane, wherein all points are calculated via DFT. (d) The calculated stacking fault energy curves of Zn and Mg generated from slab shear and alias shear. (For interpretation of the references to color in this figure legend, the reader is referred to the web version of this article.)

The w_x (or w_z) is the half-width of the edge (or screw) component of the two partial dislocations ("partial core width" for short). As illustrated in Fig. 2a, these length scales can be readily defined from the misfit density $\rho(x)=du(x)/dx$, i.e., the gradient of the disregistry in the x or z direction. The shape of the trial displacements u(x) in Eq. (5) is obtained by minimizing the total energy E_{tot} [80,81] via the particle swarm optimization (PSO) scheme [82].

The γ -surface on the basal plane is given as a continuous sixterm, truncated 2-D Fourier series function [83]:

$$\gamma(u_{x}, u_{z}) = c_{0} + c_{1}[\cos(2qu_{z}) + \cos(pu_{x} + qu_{z}) + \cos(-pu_{x} + qu_{z})]
+ c_{2}[\cos(2pu_{x}) + \cos(pu_{x} + 3qu_{z}) + \cos(-pu_{x} + 3qu_{z})]
+ c_{3}[\cos(4qu_{z}) + \cos(2pu_{x} + 2qu_{z}) + \cos(pu_{x} - 2qu_{z})]
+ c_{4}\begin{bmatrix} \cos(3pu_{x} + qu_{z}) + \cos(3pu_{x} - qu_{z}) + \cos(2pu_{x} + 4qu_{z}) \\ + \cos(2pu_{x} - 4qu_{z}) + \cos(pu_{x} + 5qu_{z}) + \cos(-pu_{x} + 5qu_{z}) \end{bmatrix}
+ a_{1}[\sin(pu_{x} - qu_{z}) - \sin(pu_{x} + qu_{z}) + \sin(2qu_{z})]
+ a_{2}[\sin(2pu_{x} - 2qu_{z}) - \sin(2pu_{x} + 2qu_{z}) + \sin(4qu_{z})], \tag{6}$$

where $p=2\pi/b$, $q=2\pi/(\sqrt{3}b)$. Among the seven coefficients, there are six that are independent, since $c_0=-3\cdot(c_1+c_2+c_3+2c_4)$, can be determined by applying the condition: $\gamma(0,0)=0$. The remaining six unknown coefficients c_1 , c_2 , c_3 , c_4 , a_1 and a_2 are related to particular points on the γ -surface, as illustrated in Fig. 1c using Eq. (6).

One quantity that is closely related to material strength is the Peierls stress, defined as the threshold stress required to move a dislocation irreversibly with a Burgers vector at 0 K [84,85] as illustrated in Fig. 2b. To calculate the Peierls stress from the structural properties of the dislocation introduced thus far, we employ the approaches proposed in [84,86], which indicates that the

Peierls stress τ_p can be evaluated using the derivative of the misfit energy:

$$\tau_p = \max\{\tau\} = \max\left\{\frac{1}{b} \frac{dE_{\text{misfit}}(\mu)}{d\mu}\right\}. \tag{7}$$

To be noted that another solution to estimate the Peierls stress within framework of the SVPN model is the direct stress method [77], in which the equilibrium dislocation structure under each certain applied stress is obtained by minimizing the total energy including the energy/work term done by the applied stress. Then as the applied stress is progressively increased, the system reaches an instability point, and the critical stress corresponds to the Peierls stress [81,87]. It is noticed that, the determination of Peierls stress by the direct stress method relies on their being an obvious instability or on the set criterion for instability, e.g., a distinct variation of dislocation cores [88-91]. It is also noted that there exist large deviations among the values of Peierls stress determined by the direct stress method, and variations in the instability criterion could possibly be responsible for this deviations. Instead, the energy derivative method defines exactly the critical point for the lattice stability based on the force-balance criterion, not depending on the methods to obtain or identify an instability signature [81,86]. For a demonstration, we have calculated the stacking fault widths and Peierls stresses for Mg, Zn, Al, Ag, and Cu according to both the direction stress method and the energy derivative method, and the results are shown in Fig. S3 and Table S4 in the Supplementary material, compared with experimental measurements. It can be clearly seen that the calculated results via the direct stress method are much larger than the experimental data, whereas those obtained by the energy derivative method show much closer. With these facts and considerations, in the present study, we adopt the energy derivative method as expressed by Eq. (7).

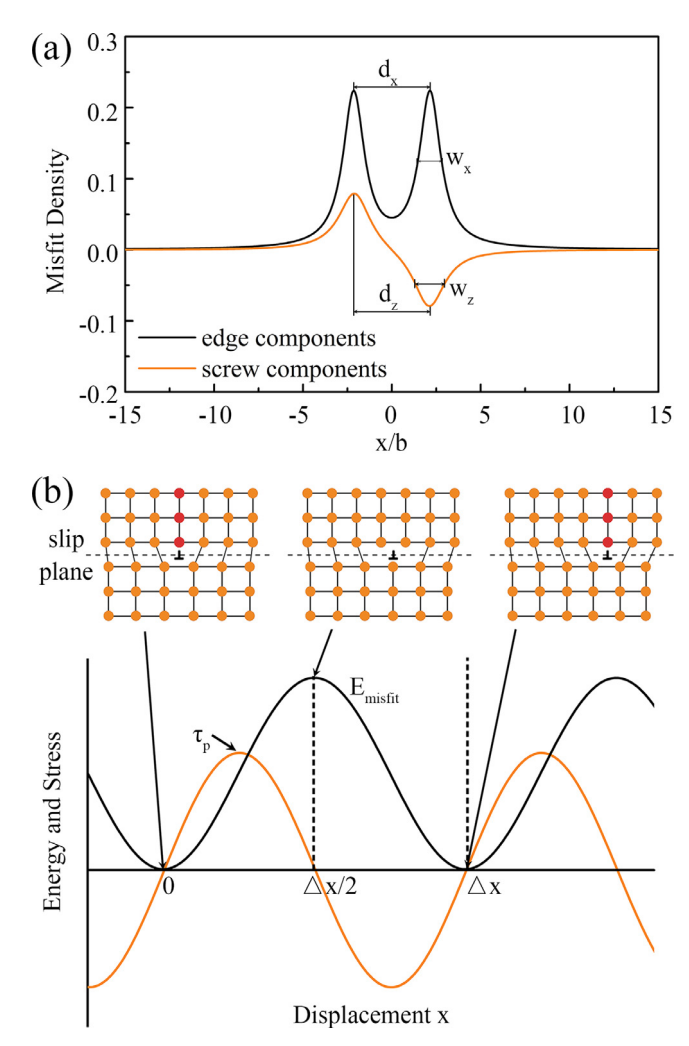


Fig. 2. (a) Misfit Density of pure Zn, which was obtained using the gradient in the disregistry $\rho(x)=du(x)/dx$. The separation d_x (or d_z) between the edge (or screw) components of the two partials is defined as the distance between these two peaks, and the width w_x (or w_z) of the edge (or screw) components of a partial dislocation is the full width at half maximum approximately. (b) A schematic showing dislocation motion from one symmetrical, ground state configuration to another equivalent one in the lattice.

3. Results

Prior to studying solute effects, the stacking fault energies and dislocation structures for pure Zn and pure Mg are calculated and checked against values previously reported. Fig. 1d presents the calculated [1 $\bar{1}$ 00] {0001} GSFE curves of pure Zn and Mg, which contain the local minimum at the stable I₂ stacking fault energy γ_{I_2} and local maximum at the unstable stacking fault γ_{UI_2} . Table 1 and Table 2 compare the values calculated here to those calculated and measured values reported elsewhere. The calculated stable I₂ stacking fault energies for Zn (107.0–109.8 mJ/m²) and Mg (32.2–37.4 mJ/m²) agree reasonably well with results from other first principles calculations (102–130 mJ/m² for Zn [56,57] and 20.1–33.85 mJ/m² for Mg [46,65,92]). Most of the DFT values, including ours, are lower than the reported experimental values (γ_{I_2} >125 mJ/m² for Zn [93], >90 mJ/m² for Mg [94]).

In order to elucidate the dislocation core structure using the semi-discrete variational P-N model, the full γ -surface needs to be calculated. *Ab initio* methods can provide the most reliable values; however, such calculations require exhaustive computational resources. To reduce the computational costs, we choose a five-point approach, as proposed in Ref. [60], in which the γ -surface

can be obtained by mathematically fitting the fault energies at five characteristic points. As validation, in Fig. S4 in the Supplementary material, in the case of pure Zn, the full basal plane γ -surface entirely calculated by DFT is compared with the parameterized γ -surface provided by the five-energy-point model. As shown, the correspondence is good, indicating the efficiency and suitability of the 5-term function for describing the full γ -surface.

With the SFE energies as input, the semi-discrete variational P-N model is employed to estimate the structural parameters of the dislocation core, which are the split distances d_x (or d_z) between the edge (or screw) components of the two partials, the partial core width w_x (or w_z), and Peierls stress. For pure Zn, we obtain $d_x/b = 3.96$, $d_z/b = 3.75$, $w_x/b = 0.73$, and $w_z/b = 1.13$. Compared to Zn, for pure Mg, we obtain larger split distances $d_x/b = 7.56$, d_z/b = 7.61, but finer partial core widths, $w_x/b = 0.53$, and $w_z/b = 0.58$. The split distance for Mg are comparable to the atomic-scale simulation results reported by Wu and Curtin [95], which are 7.0b for basal partial split distance by DFT calculation and 12.5b by MEAM potential. For comparison, the split distances expected from linear elastic dislocation theory, $d = Gb^2/4\pi \gamma_{l_2}$ [96], is calculated, giving 7.4b and 15.4b for Zn and Mg, respectively. The larger split distances of Mg than those of Zn, seen in the P-N calculation, arise from the lower value of γ_{l_2} of Mg, as anticipated in the analytical linear elasticity dislocation model.

The Peierls stresses calculated here are also in agreement with prior calculations as shown in Tables 3 and 4. It is well known that in both Zn and Mg, basal slip is preferred [97], and we have quantified that the Peierls stress of a basal edge dislocation in Zn (0.53 MPa) is substantially lower than that in Mg (9.23 MPa).

3.1. Solute effects in Zn-based and Mg-based alloys

To improve the mechanical strength of Zn-based and Mg-based alloys, the effects of six biocompatible alloying elements-Li, Al, Mn, Fe, Cu, and either Mg in a Zn solvent or Zn in a Mg solvent are considered in the calculation of the SFE. Fig. 3a and b shows the [1100] 0001 SFE profiles for the resulting alloys, $Zn_{47}X$ and Mg₄₇X, and Tables 1 and 2 list the stable and unstable I₂ stacking fault energies (γ_{I_2} and γ_{UI_2}) as calculated here, for Zn-based and Mg-based alloys, separately. Results reported in other studies, including simulation results and experiment results, are also listed for comparison. For the Zn-based alloys, the γ_{l_2} values of Zn₄₇X for all solute additions "X" are lower than that of pure Zn except for Zn₄₇Cu. In comparison, for the Mg-based alloys, elements Zn, Al, Fe and Mn decrease γ_{l_2} compared to pure Mg, while elements Cu and Li increase γ_{l_2} . Alloying is generally expected to lower the intrinsic stacking fault energy. The two findings that may not be expected, however, are the opposing effect of Li, which decreases γ_{l_2} in Zn but increases it in Mg, and the stronger sensitivity to the alloying additions in Zn than Mg for the same alloying element. When introducing Fe, for instance, γ_{l_2} of Zn has a 58.6% decrease from 107.0 mJ/m² to 44.3 mJ/m², while γ_{I_2} of Mg only has a 48.7% decrease from 37.4 mJ/m² to 19.2 mJ/m². We discuss explanations for this finding later in Section 3.4.

Using the *ab initio* calculated γ -surfaces and elastic properties for these Zn-based and Mg-based alloys, the semi-discrete variational P-N model is used to estimate the characteristic length scales of the basal dislocation cores and their Peierls stresses. The effects of three elements, Fe, Cu, and either Mg in Zn or Zn in Mg, are examined. Fig. 3c and d presents the misfit densities, from which we define the split distances d and partial core widths w, along and normal to the dislocation line, for Zn and Mg, respectively, and Tables 3 and 4 list the corresponding edge dislocation split distances, partial core widths, and Peierls stresses. Compared to pure Zn, Zn₄₇Fe and Zn₄₇Mg have larger d_x and d_z , while Zn₄₇Cu has similar d_x and d_z . These effects can be attributed to the lower

Table 1 Calculated stable (γ_{l_2}) and unstable (γ_{Ul_2}) stacking fault energies of Zn and Zn₄₇X. x_{global} % and x_{SF} % indicate the global atomic percent and the atomic percent within the stacking fault (SF) plane, respectively.

	Source	$x_{ m global}\%$	x _{SF} %	γ_{I_2}	γ_{UI_2}	Note
Pure Zn	This work			107.0	131.2	This work, alias shear, VASP, GGA-PBE
				109.8	126.2	This work, slab shear, VASP, GGA-PBE
	Cal. [57]			102	120	VASP, GGA-PW91, SGGA-PW91
	Cal. [56]			109		VASP, GGA-PBE
	Cal. [123]			130		WIEN2K, LSDA
				100		WIEN2K, GGA-PBE
	Exp. [93]			>125		0, 17, and 41 °C
Zn ₄₇ Li	This work	2.08	25	94.5	113.9	This work, alias shear, VASP, GGA-PBE
Zn ₄₇ Mg	This work	2.08	25	83.7	103.5	This work, alias shear, VASP, GGA-PBE
Zn ₄₇ Al	This work	2.08	25	28.9	61.2	This work, alias shear, VASP, GGA-PBE
Zn ₄₇ Mn	This work	2.08	25	18.2	104.8	This work, alias shear, VASP, GGA-PBE
Zn ₄₇ Fe	This work	2.08	25	44.3	134.5	This work, alias shear, VASP, GGA-PBE
Zn ₄₇ Cu	This work	2.08	25	112.3	145.5	This work, alias shear, VASP, GGA-PBE

Table 2 Calculated stable (γ_{l_2}) and unstable (γ_{Ul_2}) stacking fault energies of Mg and Mg₄₇X. x_{global} % and x_{SF} % indicate the global atomic percent and the atomic percent within the stacking fault (SF) plane, respectively.

	Source	$x_{global}\%$	$x_{SF}\%$	γ_{I_2}	γ_{UI_2}	Note
Pure Mg	This work			37.4	95.5	This work, alias shear, VASP, GGA-PBE
				32.2	91.8	This work, slab shear, VASP, GGA-PBE
	Cal. [46]			33.85	93.57	Alias shear, GGA-PBE
	Cal. [65]			20.1	95.8	CASTEP, slab shear, GGA-PW91
	Cal. [92]			33.8	87.6	VASP, slab shear, GGA-PW91
	Exp. [94]			>90		
Mg ₄₇ Li	This work	2.08	25	50.6	100.0	This work, alias shear, VASP, GGA-PBE
	Cal. [20]	1.04	8.33	35.6	88.8	VASP, alias shear, GGA-PBE
	Cal. [124]	1.67	50	46	93	CINEB-DFT methods
Mg ₄₇ Al	This work	2.08	25	21.7	81.0	This work, alias shear, VASP, GGA-PBE
	Cal. [46]	2.08	25	22.50	87.62	VASP, alias shear, GGA-PBE
	Cal. [20]	1.04	8.33	29.4	84.0	VASP, alias shear, GGA-PBE
	Cal. [124]	1.67	50	23	83	CINEB-DFT methods
Mg ₄₇ Mn	This work	2.08	25	35.6	103.8	This work, alias shear, VASP, GGA-PBE
	Cal. [20]	1.04	8.33	46.1	98.0	VASP, alias shear, GGA-PBE
Mg ₄₇ Fe	This work	2.08	25	19.2	88.6	This work, alias shear, VASP, GGA-PBE
	Cal. [125]	2.08	25	52	110	VASP, GGA-PBE
Mg ₄₇ Cu	This work	2.08	25	50.2	89.4	This work, alias shear, VASP, GGA-PBE
	Cal. [20]	1.04	8.33	35.3	81.4	Alias shear, GGA-PBE
	Cal. [125]	2.08	25	53	97	VASP, GGA-PBE
Mg ₄₇ Zn	This work	2.08	25	33.6	83.9	This work, alias shear, VASP, GGA-PBE
	Cal. [20]	1.04	8.33	31.1	81.9	Alias shear, GGA-PBE
	Cal. [46]	2.08	25	31.64	85.43	Alias shear, GGA-PBE

Table 3 Geometrical parameters of dislocation core structure and the calculated Peierls stress (τ_p) in MPa of Zn and its alloys.

	d _x /b	w _x /b	d _z /b	w _z /b	τ_{p}	NOTE
Pure Zn	3.96	0.73	3.75	1.13	0.53	This work, DFT
					0.76	Ref. [126], Exp
					<1.0	Ref. [127], Exp
$Zn_{47}Mg$	4.98	0.69	5.03	0.91	3.22	This work, DFT
Zn ₄₇ Fe	10.69	0.62	10.67	0.71	8.77	This work, DFT
$Zn_{47}Cu$	3.90	0.68	3.76	0.93	2.94	This work, DFT

value of the stable SFE γ_{l_2} for Zn₄₇Fe (44.3 mJ/m²) and Zn₄₇Mg (83.7 mJ/m²), and similar stable SFE for the Zn₄₇Cu (112.3 mJ/m²) compared to pure Zn (107.0 mJ/m²). The widths of the two partials that bound the stacking fault are also influenced by alloying. According to our analysis, all alloying elements in Zn cause the partial core widths w_x and w_z to shrink compared to those in pure Zn, especially Fe.

Calculations in Fig. 3d and Table 4 show that compared to the Zn-based alloys, the core structures for the Mg-based alloys are more sensitive to alloying additions. Unlike in Zn, the addition of Cu in Mg noticeably shrinks the split distances and Zn and Fe increase them. For the same alloying element, the Mg-based alloy

Table 4 Geometrical parameters of dislocation core structure and the calculated Peierls stress (τ_p) in MPa of Mg and its alloys.

	$d_{\rm x}/b$	w_x/b	d_z/b	w_z/b	$ au_{ m p}$	NOTE
Pure Mg	7.56	0.53	7.61	0.58	9.23	This work, DFT
	7.50	0.54	7.56	0.58	8.40	Ref. [46] Cal. DFT
	7.00	0.68	7.18	0.60	1.15	Ref. [60] Cal. DFT
					6.73	Ref. [126] Exp.
Mg ₄₇ Fe	13.92	0.55	13.96	0.59	11.10	This work, DFT
Mg ₄₇ Cu	5.86	0.58	5.87	0.65	7.55	This work, DFT
$Mg_{47}Zn$	8.68	0.59	8.72	0.65	2.53	This work, DFT
	7.60	0.56	7.65	0.62	2.61	Ref. [46] Cal. DFT

possesses a larger d_X and d_Z than those in Zn alloy, which, again, can be simply accounted for by the relatively lower values of γ_{I_2} in Mg compared to Zn. For the partial core widths of the individual partials, solutes Zn, Fe and Cu all lead to larger values of w_X and w_Z than pure Mg.

Tables 3 and 4 also list the estimates for the Peierls stress. For Zn, the Peierls stress in pure Zn is exceedingly low (only 0.53 MPa) and the addition of any of these three solute elements, Cu, Fe, and Mg, leads to a higher basal plane Peierls stress. The amount of strengthening, however, is sensitive to the solute, with Fe making a 1554.7% enhancement from 0.53 MPa to 8.77 MPa. In contrast, pure

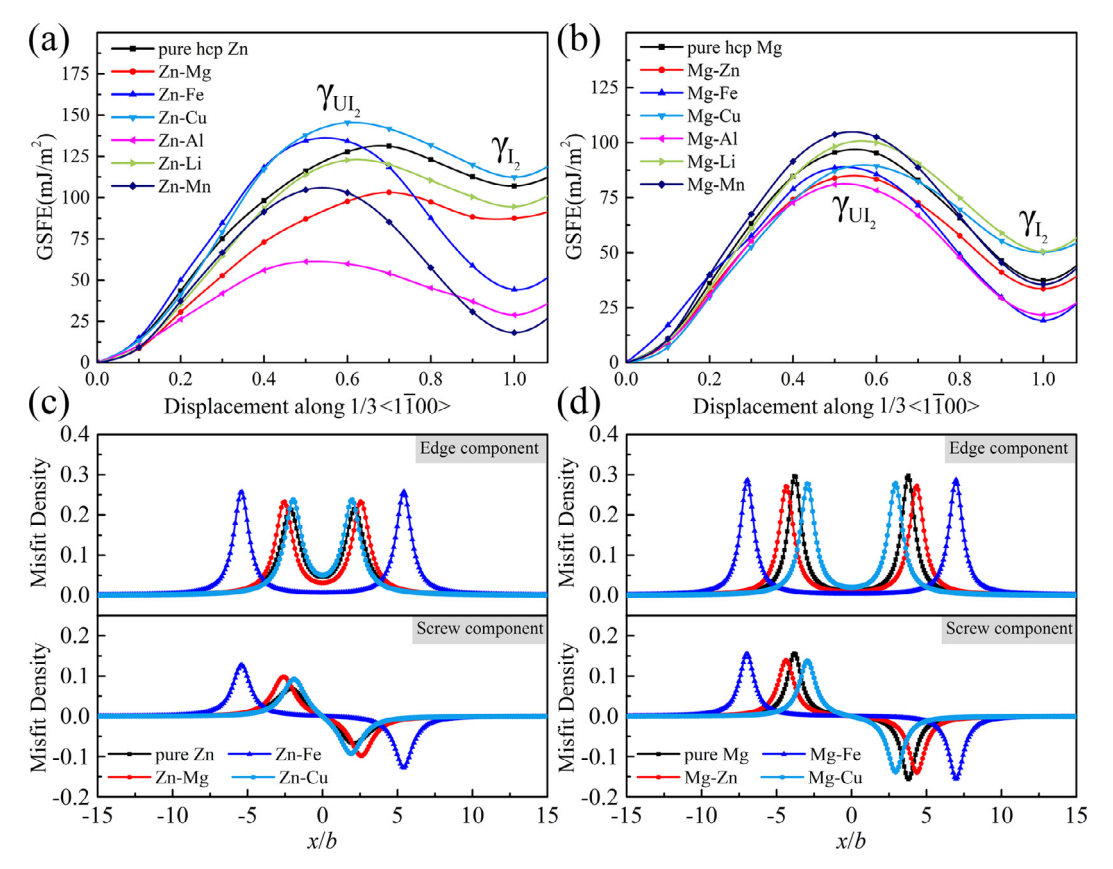


Fig. 3. (a) Generalized stacking fault energy (GSFE) curves of pure Zn and its alloys (Mg, Al, Cu, Li, Mn, Fe are alloying elements). (b) GSFE curves of pure Mg and Mg-based alloys (Zn, Fe, Cu are alloying elements). The γ_{l_2} are marked in the figures. The dislocation structure is defined based on the misfit density. (c) The misfit density of pure Zn, Zn-Mg, Zn-Fe and Zn-Cu and (d) for comparison, the corresponding Mg-based alloys.

Mg has a Peierls stress that is an order of magnitude higher than that of pure Zn. As another notable distinction, solute additions in Mg do not necessarily lead to a rise in Peierls stress. The addition of Fe favorably leads to an increase in the Peierls stress for 20.3%; however, addition of either Zn or Cu results in a noticeable drop for 72.6% and 18.2%, separately.

The effects of solute Mg in solvent Zn and solute Zn in the solvent Mg have been investigated previously in both theoretical and experimental studies [46]. Using DFT, Tsuru and Chrzan [98] showed that Zn effects slightly on the projected density of states of Mg. In agreement, this work finds that Zn only decreases γ_{l_2} of Mg 10.2% from 37.4 mJ/m² to 33.6 mJ/m², much less than the effect of Cu and Fe, which are 34.2% and 48.7%, respectively. Experimentally, it is found that the strength of Zn was profoundly enhanced when alloyed by Mg [29]. In congruence, the analysis here indicates that Mg added to Zn would lead to a higher Peierls stress in Zn.

In this work, we consider a dilute solute effect and two contributions to solute strengthening. Another contribution to solute strengthening is the direct interaction between dislocations and solute atoms. In the particular case of the Mg–Zn alloy, we found a lower Peierls stress for the Mg–Zn alloy compared to pure Mg, which is inconsistent with experimental observations, a discrepancy that may be explained by a strong influence of solute–dislocation interaction. By means of a solid-solution strengthening model proposed by Leyson et al. [99–101], a strengthening $\Delta\tau_{\rm CRSS}/c^{2/3}$ of 251 MPa (c represents the solute concentration) to overcome the solute–dislocation interaction is calculated when solute Zn is introduced into Mg-based alloys. This result indicates that simply including solute effects on the SFE in the P-N model may not be sufficient for solute strengthening effects,

and a further consideration of the solute-dislocation interaction is necessary.

To examine the effect of solutes on ductility, the split distances of the basal cores in these alloys are analyzed. A decreased split distance due to alloying can promote dislocation processes for overcoming obstacles, such as cross slip of screw dislocations, climb of dislocations of edge dislocations, required to keep dislocations in motion, stimulating ductility [102]. It is, thus, significant that the calculations identify that Cu additions in Zn would not affect the split distances appreciably but increase the Peierls stress. The implication is that Cu would strengthen Zn without lowering its ductility. For Mg, the calculations also find benefits when alloying with Cu. Cu additions to Mg significantly reduces the split distance, suggesting that Cu could increase the ductility of Mg. The solute Cu is generally used for alloying due to its inhibitory effects on bacterial and fungal growth [103]. The calculations here suggest that the solute Cu can have structural benefits as well.

Solute Fe additions have garnered much attention recently due to reports of profound strengthening in Zn-based alloys [35,104]. Here our calculations show that Fe is the one element that increases the Peierls stress for both Zn and Mg.

3.2. Hydrostatic pressure effects in Zn-based and Mg-based alloys

The influence of solute elements on dislocation cores and Peierls stress can change for applied pressures in excess of ± 1 GPa. In this section, we examine how solute additions affect the response of stacking fault energies and dislocation core structures to large hydrostatic pressures, ranging from negative pressures of -3 GPa (tension, causing positive dilatation $\Delta V/V$) to positive

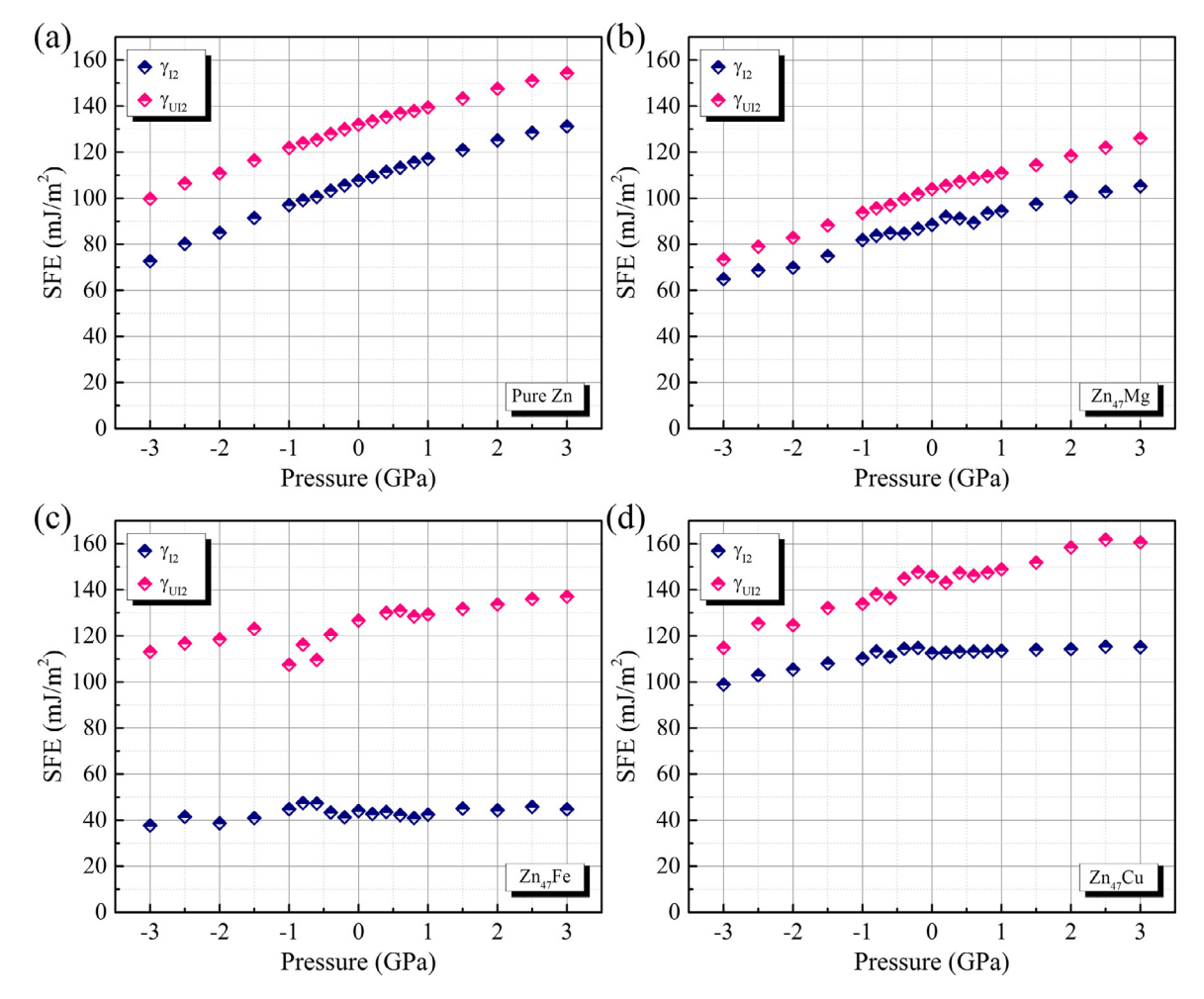


Fig. 4. γ_{l_2} and γ_{Ul_2} of pure Zn, Zn₄₇Mg, Zn₄₇Fe, and Zn₄₇Cu as a function of different applied pressures ranging from -3 GPa to +3 GPa. Negative pressure means hydrostatic tension and positive pressure means hydrostatic compression.

pressures up to +3 GPa (compression, resulting in negative dilatation $\Delta V/V$).

The *ab-initio* fault energy calculations for the basal plane are repeated under a specific pressure. The expectation is that compressive state would increase the energy to shear the two crystalline halves and vice versa for a tensile state. Fig. 4 presents the variations of γ_{I_2} and γ_{UI_2} of pure Zn and Zn-based alloys under pressures ranging from -3 GPa to +3 GPa, corresponding to dilatations $\Delta V/V$ ranging from -0.031 to 0.023. As anticipated, with increasing pressure, the SFEs of pure Zn, Zn₄₇Mg and Zn₄₇Cu increase. Interestingly, however, increasing pressure has a relatively minor impact on γ_{I_2} of Zn₄₇Fe.

For comparison, the SFEs of pure Mg and Mg-based alloys under the same pressure range are calculated (see Fig. S5 in the Supplementary material). For pure Mg, the SFEs for all Mg alloys decrease relative to the zero-pressure value when the pressure is negative and increase as the applied pressure increases to +3 GPa. The pressure has the least impact for the solute Fe in Mg, but unlike in Zn, it still has an effect. Moreover, for all alloying elements studied, Mg is, however, less sensitive to pressure than Zn. Over the $-1\,\mathrm{GPa}$ to +1 GPa pressure range, γ_{l_2} for both metals scales approximately linearly with pressure but the scaling factor is 10.2 for Zn, which is three times higher than 3.5 for Mg.

By incorporating the calculated γ -surface into the P-N model, as described in Eqs. (2) and (3), the dislocation structures of pure Zn under different pressures can be obtained. From the misfit den-

sities shown in Fig. 5a, we see that the value of d_x/b rises to 6.71 when applying a pressure of -3 GPa, whereas it reduces to 3.60 under a pressure of +3 GPa. Fig. 5b and 5c provides the dislocation structure of Zn-based alloys under different pressures, and for comparison, those results for Mg and Mg-based alloys are presented in Fig. 5d-f. In the case of pure Mg, under volume strain ranging from $-0.06 \le \Delta V/V \le 0.10$, the split distance d_x/b varies from 5.52 to 13.85 and the partial core width w_x/b , from 0.45 to 0.69, consistent with results in [46] reported as 4.82–16.67 for d_x/b , and 0.41–0.77 for w_x/b , when $-0.12 \le \Delta V/V \le 0.13$. It can be found that a general pressure-dependence can be clearly identified for both Zn-based and Mg-based alloys, i.e., the negative pressure (i.e., the positive volumetric strain) leads to larger values of d_x/b and w_x/b , while the positive pressure (i.e., the negative volumetric strain) leads to smaller values of d_x/b and w_x/b .

Higher positive pressures can be expected to increase the Peierls stress and vice versa for higher negative pressures. Table 5 summarizes the combined effect of alloying and pressure on the Peierls stress for both Zn-based and Mg-based alloys. For example, the Peierls stress of pure Zn $(Zn_{47}Mg)$ is about 0.53 MPa $(3.22\,MPa)$ at zero pressure, which increases to 0.84 MPa $(1.97\,MPa)$ under a pressure of $+3\,GPa$ and decreases to 0.13 MPa $(0.41\,MPa)$ under a pressure of $-3\,GPa$. Positive-pressure enhancement of the Peierls stress is seen here to be more profound for Mg-based alloys than the Zn-based alloys. For instance, for the Mg alloy $(Mg_{47}Zn)$, the value of about 9.23 MPa $(2.53\,MPa)$ at equilibrium increases signif-

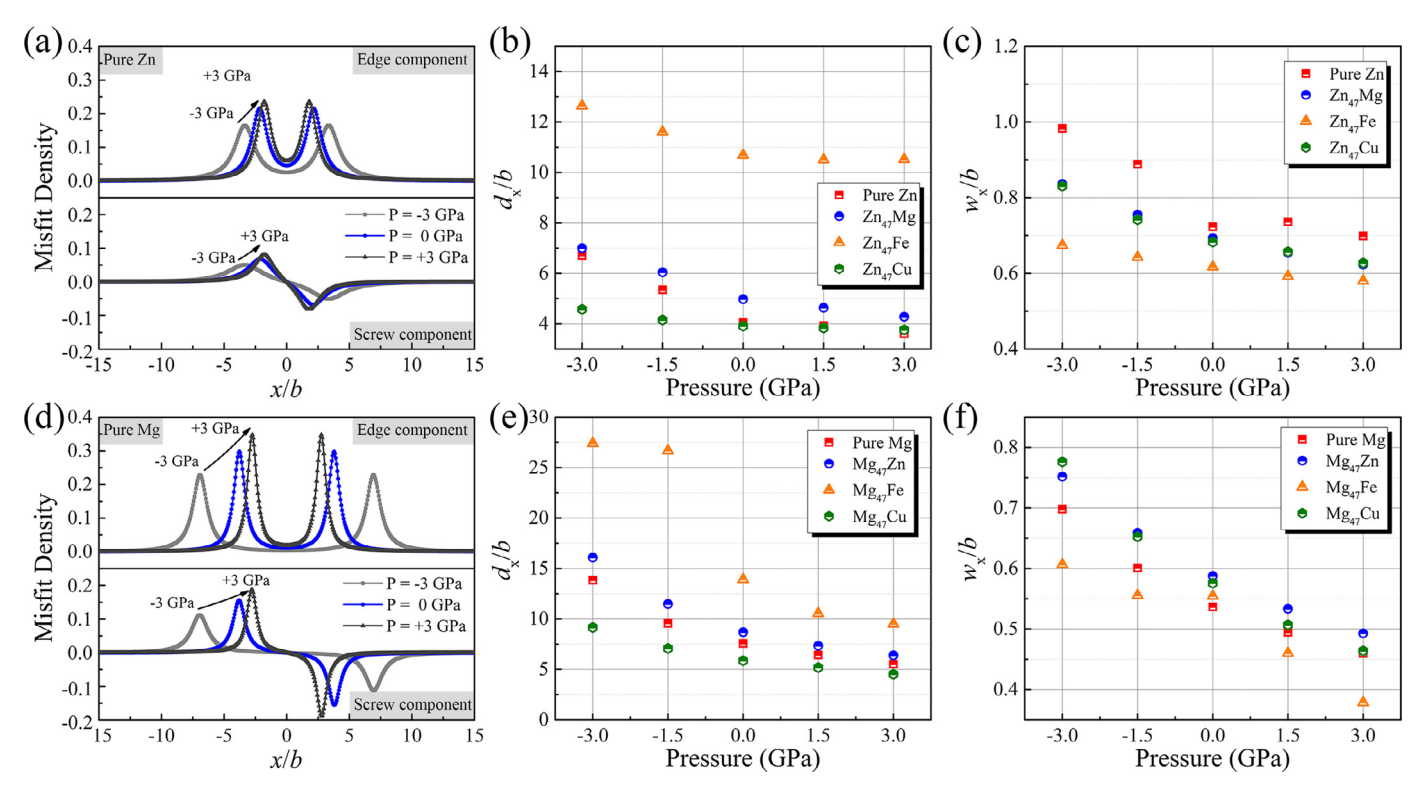


Fig. 5. (a) Misfit density of pure Zn produced by the dislocation under different pressures. (b) and (c) show the d_x/b and w_x/b variation under certain pressures for Zn. (d) to (f) show the dislocation structure variation of pure Mg and Mg-based alloys for comparison.

Table 5The calculated Peierls stress (in MPa) for Zn-based and Mg-based alloys under certain pressures or longitudinal strains.

	Hydrostatic pressure			Longitudinal s	Longitudinal strain (Mode I)			Longitudinal strain (Mode II)		
	P = -3 GPa	P = 0 GPa	P = +3 GPa	$\varepsilon = -0.05$	$\varepsilon = 0$	$\varepsilon = +0.05$	$\varepsilon = -0.05$	$\varepsilon = 0$	$\varepsilon = +0.05$	
Pure Zn	0.13	0.53	0.84	0.19	0.53	0.004	0.77	0.53	0.02	
Zn ₄₇ Mg	0.41	3.22	1.97	2.00	3.22	0.35	8.48	3.22	0.13	
Zn ₄₇ Fe	5.35	8.77	27.02	39.53	8.77	4.48	33.69	8.77	5.71	
Zn ₄₇ Cu	0.44	2.94	1.50	0.30	2.94	0.06	6.03	2.94	0.004	
Pure Mg	1.08	9.23	49.20	57.57	9.23	1.51	91.84	9.23	0.92	
Mg ₄₇ Zn	0.61	2.53	28.55	53.66	2.53	0.09	56.19	2.53	0.96	
Mg ₄₇ Fe	5.25	11.10	242.58	99.22	11.10	14.53	363.87	11.10	5.16	
Mg ₄₇ Cu	0.45	7.55	54.00	45.25	7.55	0.63	74.49	7.55	0.50	

icantly to $49.20 \,\text{MPa}$ (28.55 MPa) under a pressure of $+3 \,\text{GPa}$ and decreases to 1.08 MPa (0.61 MPa) under a pressure of $-3 \,\text{GPa}$.

3.3. Longitudinal strain effects in Zn-based and Mg-based alloys

We next study the effect of longitudinal strain on the stable SFEs of Zn, Mg and their alloys. There are several ways to apply a longitudinal strain in first principles calculations [70,105]. One method models uniaxial strain, which involves rescaling the cell dimension in one axis direction, e.g., the z direction, while keeping the other two orthogonal dimensions fixed (e.g., the x and y directions). A second way considers uniaxial stress, wherein a positive strain ε is applied in one axis direction, e.g., in the z direction, while rescaling the cell dimensions along the x and y directions to enforce zero stress in these directions, i.e., referred to as applying the Poisson's contraction [106]. A final way we mention enforces volume conservation. It applies a positive strain ε in one direction, e.g., the z direction, while providing strains $-\varepsilon/2$ in the other two orthogonal directions, such that volume is conserved. It is seen that the first method ignores the Poisson's contraction, while the uniaxial-stress and volume-conserving methods consider the Poisson's contraction with flexible and constant magnitudes, respectively. In the following calculations, the uniaxial stress and uniaxial strain conditions will be used to apply longitudinal strains. We abbreviate these two cases as "Mode I" and "Mode II", respectively. Fig. 6 illustrates the relevant results generated by these methods with and without the Poisson's contraction.

Fig. 6 presents the calculated γ_{l_2} and γ_{Ul_2} of pure Zn, Zn₄₇Mg, Zn₄₇Fe and Zn₄₇Cu as a function of longitudinal strains ε ranging from -0.05 to +0.05 in Mode I and Mode II. It is seen from Fig. 6a that for Zn, longitudinal straining results in a change in the c/a ratio, from 1.724 to 1.962 in Mode I and from 1.755 to 1.940 in Mode II. Fig. 6b shows the corresponding stresses along the longitudinal z direction for pure Zn. The stress generated from Mode I is generally lower than that from Mode II, a consequence of the constraint of the triaxial strains generated in the latter case.

For pure Zn and Zn₄₇Mg, Fig. 6c and d presents the calculated variations of γ_{l_2} and γ_{Ul_2} under different ε . They reveal that both elongation and compression along the z axis decrease γ_{l_2} in pure Zn and Zn₄₇Mg by Mode I and Mode II. The γ_{Ul_2} obtained by Mode I follows a similar non-linear trend as γ_{l_2} , i.e., first rising and then falling, whereas the γ_{Ul_2} obtained by Mode II shows the linearly

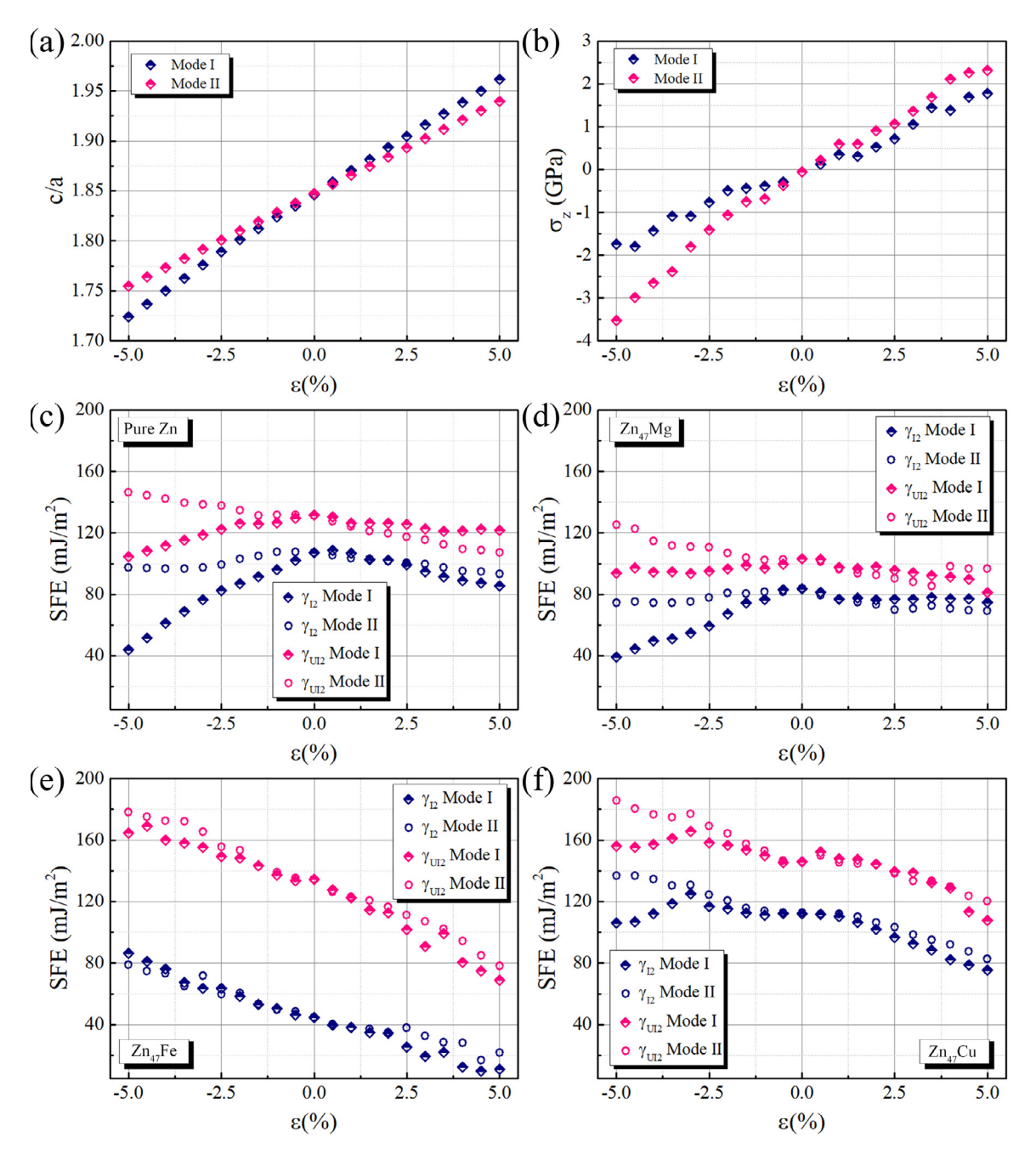


Fig. 6. (a) c/a value under different longitudinal strains in Mode I and II; (b) stress along z axis σ_z under different longitudinal strains in Mode I and II, and (c-f) γ_{I_2} and γ_{UI_2} of pure Zn, Zn₄₇Mg, Zn₄₇Fe, and Zn₄₇Cu as a function of longitudinal strains in Mode I and II.

decreasing trend over the entire strain range. For $Zn_{47}Fe$ (see Fig. 6e), as ε changes from -0.05 to +0.05, the γ_{l_2} and γ_{UI_2} decrease linearly by both Modes I and II, indicating that Poisson contraction does not influence the trends for $Zn_{47}Fe$. Last, for $Zn_{47}Cu$, it is observed in Fig. 6f that γ_{l_2} and γ_{UI_2} first reach a peak value at $\varepsilon=-0.03$ and then decrease with increasing ε . It is worth noting that, when the longitudinal strains deviate slightly from this critical strain (e.g., $\varepsilon=-0.01$ to $\varepsilon=+0.01$), a plateau is observed in the γ_{l_2} curve in $Zn_{47}Cu$ with the fault energy changing within $2 m]/m^2$.

To aid comparison, the stacking fault energies of pure Mg and its alloys under different longitudinal strains are evaluated by the same schemes as used for Zn-based alloys, and the results are provided in Fig. S6 in the Supplementary material. It is seen that the SFEs of pure Mg and most Mg-based alloys decrease proportion-

ally with longitudinal straining, unlike the non-linear relationship observed in pure Zn and Zn-based alloys. Such differences might be attributed to their intrinsic differences c/a ratio and anisotropic elasticity.

Next, we consider the effects of strain on the core structures, and to begin, we first present in Fig. 7a the calculated dislocation core structures in terms of the misfit density profiles in pure Zn under different longitudinal strains ($\varepsilon = -0.05$, $\varepsilon = 0$ and $\varepsilon = +0.05$). It can be seen that the pure Zn has the minimum value of the d_X and w_X when at equilibrium. When positive or negative longitudinal strains are applied, the d_X and w_X of pure Zn increase accordingly.

For the alloys, Fig. 7b and c shows the variation of d_x/b and w_x/b under certain strains for Zn-based alloys, and Fig. 7d-f for the Mg-based alloys. For most Mg-based alloys, the values of the d_x/b

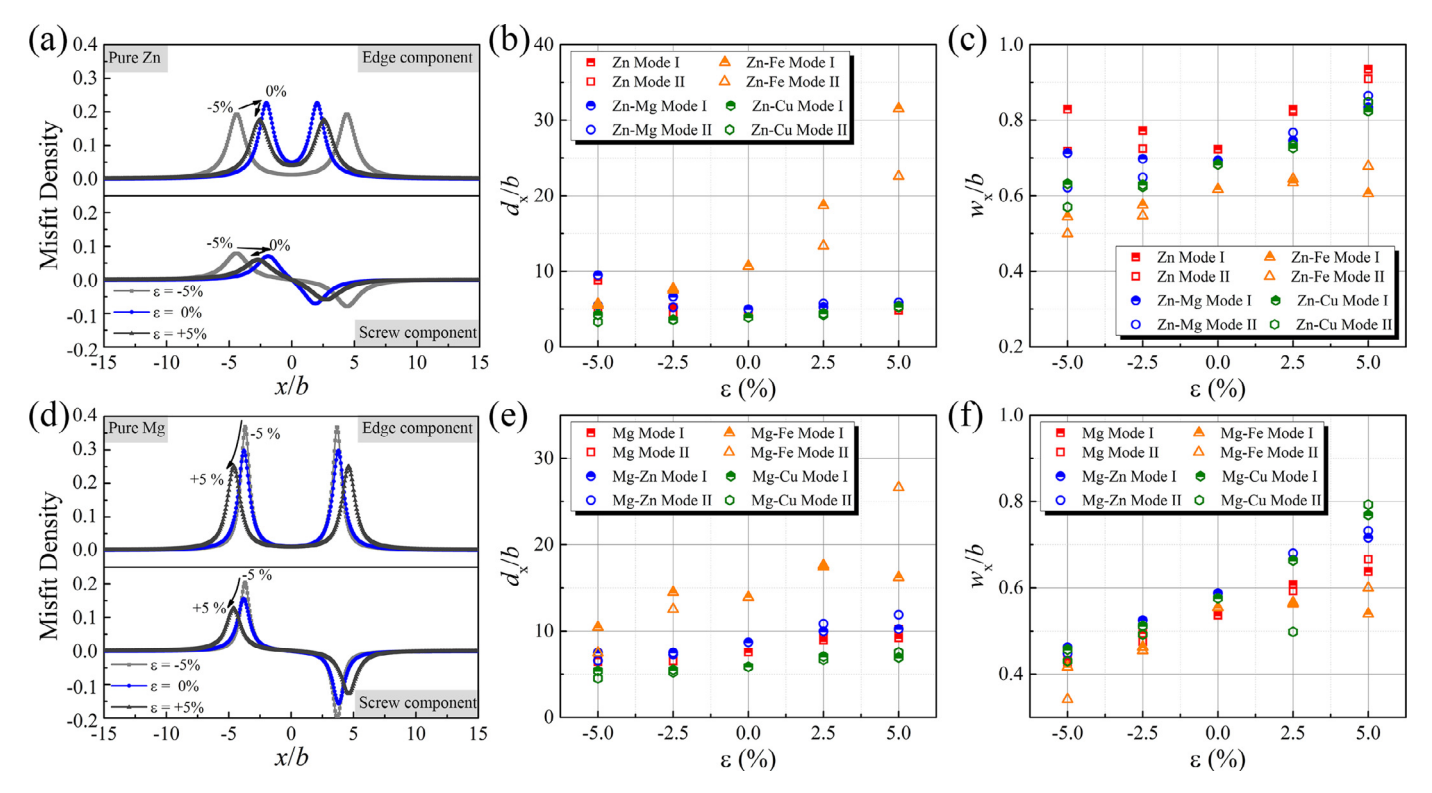


Fig. 7. (a) Misfit density of pure Zn produced by the dislocation under different longitudinal strains. (b) and (c) show the d_x/b and w_x/b variation under certain strains for Zn. (d)–(f) present the dislocation structure variation of pure Mg and Mg-based alloys for comparison.

and w_x/b increase as ε increases. However, for Zn-based alloys, a non-linear trend could be found in pure Zn and Zn₄₇Mg. For alloying element Fe, a large dislocation dissociation is found for both Zn₄₇Fe and Mg₄₇Fe at $\varepsilon=+0.05$. In Mode II, the value of d_x/b for Zn₄₇Fe (Mg₄₇Fe) increases from 5.71 (7.49) to 22.59 (26.64) as ε changes from -0.05 to +0.05, revealing a large strain dependence in both Zn₄₇Fe and Mg₄₇Fe.

The variations in SFEs caused by longitudinal straining will lead to a modification in the Peierls stress. Table 5 compares the Peierls stresses under the condition of Mode II. The analysis finds that the Peierls stress for pure Zn (Zn₄₇Mg) increases from 0.53 MPa (3.22 MPa) to 0.77 MPa (8.48 MPa) under a longitudinal compression strain of -0.05, while it reduces to $0.02 \,\mathrm{MPa}$ (0.13 MPa) under longitudinal tensile strain of +0.05. Like the pressure-enhanced Peierls stresses seen earlier, a larger strain enhancement is observed for pure Mg and Mg-based alloys. The Peierls stress of pure Mg (Mg₄₇Zn) increases from 9.23 MPa (2.53 MPa) to 91.84 MPa $(56.19 \,\mathrm{MPa})$ under a longitudinal compression strain of -0.05, while it decreases to 0.92 MPa (0.96 MPa) under longitudinal tensile strain +0.05. These results indicate that the longitudinal strain may effectively modify the strength of Zn-based and Mg-based alloys by varying the axial ratio c/a. Further, if under longitudinal compression, the Peierls stress of the basal dislocation increases, activation of non-basal slip systems could be promoted and potentially enhance ductility [107, 108].

3.4. The bond-length variations and electronic origin of solute effects

Solute effects can be revealed more vividly by studying the variations of bond lengths around the faulted region of the dislocation core. Zn has a very small <a>-axis length of 2.667 Å, much smaller than that of Mg (3.192 Å). When the same solutes are added to Zn, a much larger volume misfit, or localized strain, is generated as compared when they are added to Mg. Qualitatively the larger lattice distortions explain the heightened solute sensitiv-

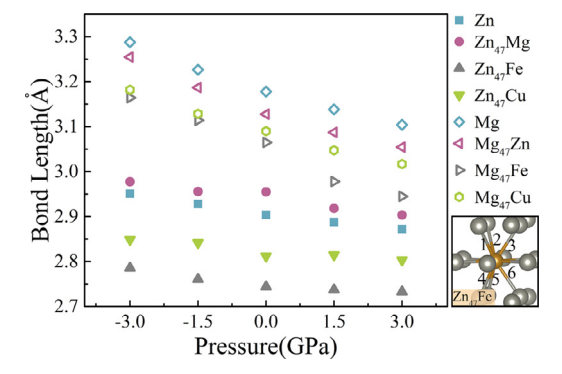


Fig. 8. The variation of the average bond lengths under different pressures of pure Zn, $Zn_{47}Mg$, $Zn_{47}Fe$, $Zn_{47}Cu$, pure Mg, $Mg_{47}Zn$, $Mg_{47}Fe$, and $Mg_{47}Cu$. The six bond lengths are measured and averaged.

ity found in the Zn-based alloys compared to that seen in the Mgbased alloys. More quantitively, we closely examine the changes in the bonds lying out of the basal plane, since when calculating the SFEs, only the direction normal to the glide plane was constrained during relaxation. Fig. 8 illustrates the bond lengths of Zn and Znbased alloys around the faulted region under different pressures, and compares with those of Mg and Mg-based alloys. For both alloys, the average out-of-plane bond length decreases as pressure increases, indicating that the bond become stronger under compression, which is consistent with our Peierls stress calculations, i.e., higher pressure results in a higher Peierls stress. For Zn-based alloys at equilibrium, Fe-Zn bonds (2.736 Å-2.744 Å) and Cu-Zn bonds (2.796 Å-2.823 Å) are \sim 5.77% and \sim 3.63% smaller than Zn-Zn bonds (2.904 Å-2.929 Å), which are smaller than Zn-Mg bonds (2.951 Å-2.981 Å). In contrast, for Mg-based alloys, all bond lengths are smaller than those of pure Mg, indicating a different localized strain in Zn and Mg induced by a same alloy element.

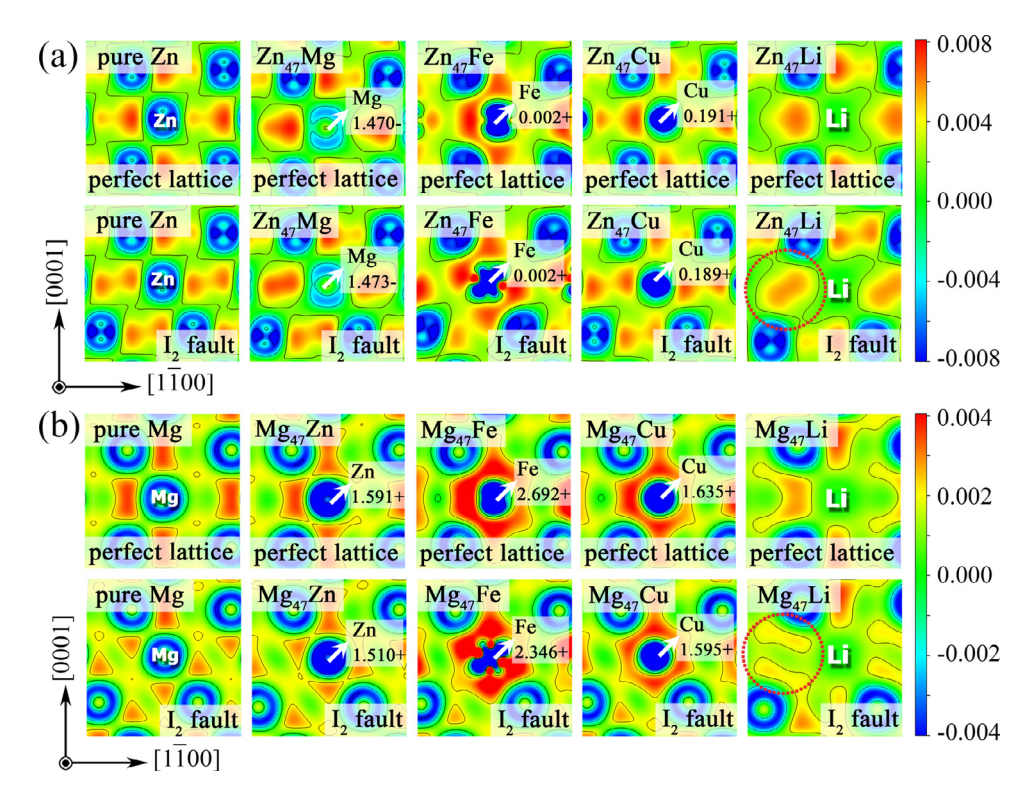


Fig. 9. Valence charge density differences (VCDD) and Bader charge analysis for pure Zn, $Zn_{47}Mg$, $Zn_{47}Fe$, $Zn_{47}Cu$, pure Mg, $Mg_{47}Zn$, $Mg_{47}Cu$ in the perfect lattice and within the I_2 stacking fault. To understand Li's inverse effect on Zn and Mg, the VCDD analysis for $Zn_{47}Li$ and $Mg_{47}Li$ in the perfect lattice and I_2 stacking fault are also provided. (For interpretation of the references to color in this figure, the reader is referred to the web version of this article.)

Such variations can be attributed to distinct features in the contour plots of the valence charge density difference (VCDD), in which the denser positive charge density suggests the stronger interatomic bonding and vice versa for the negative charge density [109]. To gain insight into the physical origin of solute effect, the VCDDs are calculated and a Bader charge analysis of Zn, Mg and their alloys are carried out. Fig. 9 illustrates the VCDD contour maps in the faulted region, which is defined as:

$$\Delta \rho(M_{47}X) = \rho inter(M_{47}X) - \rho non-inter(M_{47}X), \tag{8}$$

where M represents Zn or Mg, and X represents solute elements. $\rho_{\rm inter}({\rm M}_{47}{\rm X})$ is the charge density of Zn-based or Mg-based alloys, and $\rho_{\rm non-inter}({\rm M}_{47}{\rm X})$ represents the reference (or non-interacting) charge density, calculated as the summation of the atomic charge densities. Several key findings arise from analyzing the VCDD:

- (1) Zn and Mg have the same valence electron number, yet when comparing the VCDD of pure Zn and pure Mg, some differences arise in their bonding properties. In the perfect lattice, a weak directional feature is shown for pure Zn, while the shape of the VCDD contours in pure Mg exhibits a directional rod-like feature [110]. In the faulted region, a minor change from the perfect lattice is found for the VCDD distribution for Zn, whereas the shape change to a dispersed, triangle-like feature occurs in the VCDD distribution of Mg. The less directional and delocalized charge distribution of Zn suggests that the solute additions and applied pressures and strains can have an observable influence on the electronic structure of Zn, causing Zn to be more sensitive to solutes and pressure/strain than Mg.
- (2) We find that when combining two elements with similar structures, the impact on the VCDD is small. Consequently, the effects of solute additions of Mg (Zn) to Zn (Mg), which are relatively similar, to the charge distribution would be smaller than the effect of additions of Fe and Cu, which are

- dissimilar from Mg or Zn, would not be the same. In the case of Mg-additions to Zn, the charge distribution of $Zn_{47}Mg$ is similar to that of pure Zn, and likewise, the charge distribution of $Mg_{47}Zn$ is similar to that of pure Mg. However, the Cu and Fe have a great impact on the charge re-distribution of Zn-based and Mg-based alloys, explaining the distinctive strain and pressure effects on the SFEs between $Zn_{47}Mg$ and those of $Zn_{47}Fe$ and $Zn_{47}Cu$.
- (3) The solute Fe behaves different under strains from all other solutes as shown in previous results, and these observations can be explained by the variations seen in the VCDD contour plots. The solute Fe produces a pronounced charge polarization around the faulted region in both Zn₄₇Fe and Mg₄₇Fe, which might explain why they respond little under strain conditions. When Fe is added, the chemical misfit dominates, and the influences of strain are comparatively less. The charge transfer observed for Mg₄₇Fe (+2.692 eV) is outstandingly strong, whereas the charge transfer seen for Zn₄₇Fe (+0.002 eV) is minor.
- (4) Fig. 9 also shows the VCDD of Zn₄₇Li and Mg₄₇Li. Close examination of these VCDDs can provide an explanation of why Li results in an opposite effect on the I₂ stacking fault of Zn and Mg, i.e., lead to an increased γ_{I2} in Mg and a decreased γ_{I2} in Zn. Substantial differences can be found in the charge distribution in the I₂ fault of Zn₄₇Li and Mg₄₇Li as highlighted in red circles. The shape of VCDD distribution of Mg₄₇Li is clearly split into two parts, while that of Zn₄₇Li remains concentrated.

4. Discussion

Solute and strain effects have been long considered effective pathways toward strengthening HCP Mg and Zn. However, in alloy design, these two effects are usually considered individually. In

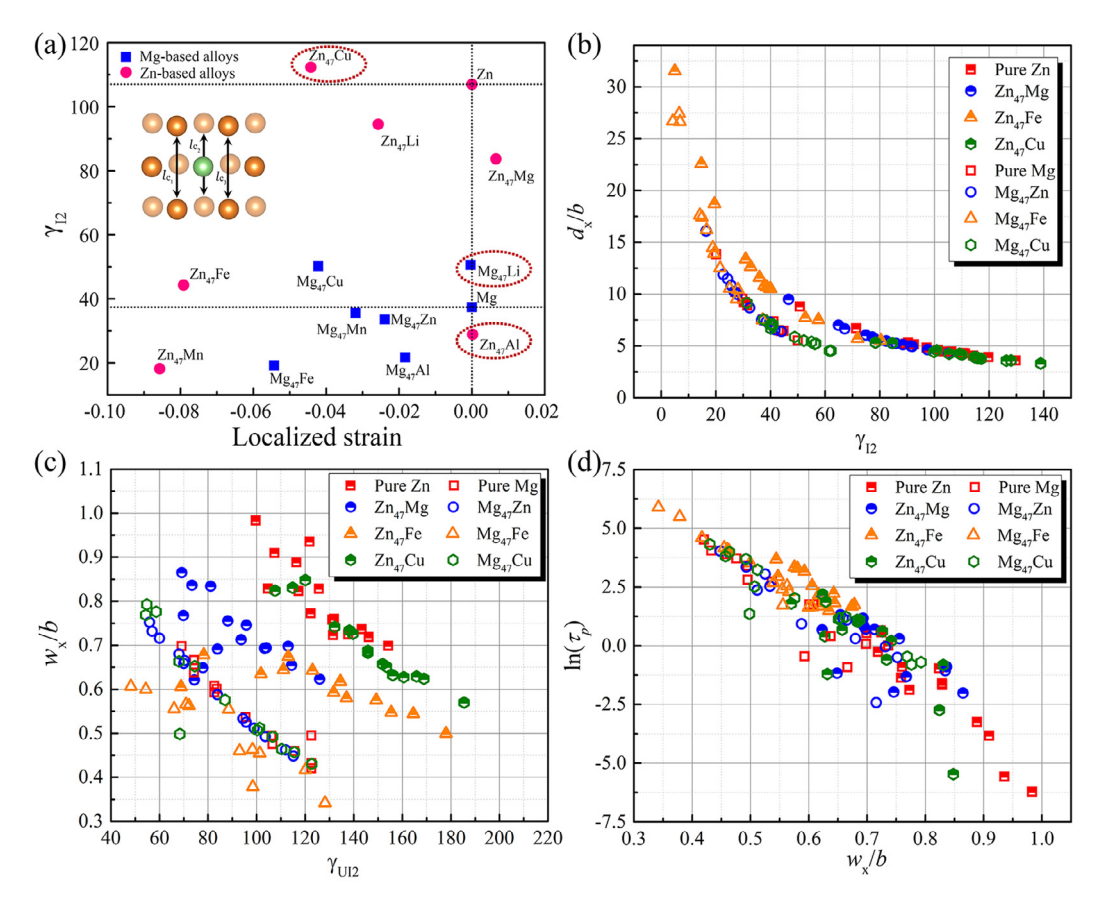


Fig. 10. (a) The relationship between localized strain and stable intrinsic stacking fault energy of Zn-based alloys and Mg-based alloys. (b) and (c) The relationship between the dislocation core structure and the SFEs. (d) The relationship between the dislocation core structure and the Peierls stress.

many ways, the results presented above indicate that solute and strain effects on strength are synergistic, and their coupled effect ought to benefit chemical design of novel materials.

In terms of substitutional solute strengthening, two general mechanisms have been discussed in the literature, the Friedel strong-pinning model for short-range interactions [111-113] and the Labusch weak-pinning model for long-range interactions [114,115]. These two models use the chemical misfit and atomic size misfit as the major input parameters [116,117]. When a large atomic size misfit exists between the solute and solution, a localized strain appears, an outcome that couples strain and chemistry at the atomic and electronic scales. From the present results, it is clearly shown that alloying influences significantly the SFEs and the bond length around solutes. To quantify for such effect, Fig. 10a presents the calculated localized strains by averaging the variations of three localized bond length via $\beta = (l_c - l_{c_M})/l_{c_M}$, where l_c represents the average relaxed bond lengths along <c>-axis of the alloys, and l_{c_M} represents lattice parameter c of the pure hcp metal. It is observed that solute elements: Fe, Mn, and Cu in Zn-based alloys induce a relatively large localized strain, indicating the existence of intrinsic synergetic effect between chemical and strain parts. Such effects have also been addressed in a few previous studies on Mg-based alloys, e.g. Shang et al. [20] revealed a nearly linear relationship between the SFE and the volume of the solutes for Mg-based alloys, and Liu et al. [118] found a strong correlation between localized c/a ratio generated by solute elements and the ductility of Mg-based alloys considering 62 types of solutes by DFT methods, suggesting a strong strain effect on solute strengthening.

Nevertheless, an interesting phenomenon is uncovered-some solutes may contribute only chemical effect without an appearance of a distinct localized strain effect or the opposite effect. As

shown in Fig. 10a, the localized strain is nearly absent for $Zn_{47}Al$ and $Mg_{47}Li$, but the introduction of solute Al in Zn (or Li in Mg) changes their SFEs from 107.0 mJ/m² (37.4 mJ/m²) to 28.9 mJ/m² (50.6 mJ/m²), suggesting that a pure chemical effect may be obtained from these particular solutes. In Fig. 6c, the results indicate that both longitudinal tension and compression lead to a lower SFE, yet for the solute Cu in Zn, the effect is to increase the SFE (as shown in Fig. 10a for $Zn_{47}Cu$) and this chemical enhancement dominates over the reductions caused by straining. These findings indicates that the synergetic effects of chemical and strain parts of solute strengthening as proposed in the previous studies [116,119] is not universal, but intrinsically dependent on the solute type.

The strain effect probed here plays the role of homogeneous lattice expansion or contraction. Yet as shown in the study of Zn-based alloys, this strain effect can be modified depending on which solute is selected. As shown in Fig. 4, the key fault energies γ_{l_2} and γ_{UI_2} of Zn, Zn₄₇Mg, and Zn₄₇Cu all increase noticeably with increasing pressure, whereas Zn₄₇Fe varies only slightly as the pressure changes. The distinctive effects of Fe can also be seen even more clearly under longitudinal strain as shown in Fig. 6. The γ_{l_2} and γ_{UI_2} of pure Zn, Zn₄₇Mg, and Zn₄₇Cu all possess a non-linear dependence. Their SFEs all first increase then decrease as longitudinal strain increases, while for Zn₄₇Fe, a linear increase is clearly observed, a result can be identified as a solute modification to the effect of strain.

The results of this work also show how strain can modify the degree and tendencies of the solute effect. A typical finding from the analysis is that the solute can have either a strengthening or weakening effects at different strain conditions. Taking Cu, Fe, and Mg in Zn-based alloys for demonstration, it is observed from Fig. 3a and c that the solute Cu may generate a higher γ_{l_2} and

a smaller d_x/b than those in pure Zn at equilibrium, while under high pressures, e.g. +3 GPa as shown in Fig. 5b, pure Zn possesses the smallest d_x/b among all Zn-based alloys. This indicates that a solute, like Cu, might behave differently at equilibrium and under a specific pressure, demonstrating a distinct and potential strain modification to solute effects.

In view of the chemical vs. mechanical strengthening methods, one may wonder if in some cases the approaches lead to similar results and hence one approach can replace the other. From our results in preceding sections, we may observe that solute effect cannot completely replace the strain effect. The solute element influences the volume and chemical environment locally and asymmetrically, while the hydrostatic pressure and longitudinal strain modify the properties continuously and of a large volume of the system or the whole system. As demonstrated in Fig. 8, the solute element changes the bond lengths around the faulted region. Hydrostatic pressure and strain can modify the intrinsic mechanical parameters continuously. As shown in Fig. 6a, a continuous variation of c/a ratio can be obtained by strain modification, while such control cannot be attained via solute modification. The effect of the shear stress component can only be investigated through the strain mode rather than solute modification. Branicio et al. [70] modulated the SFEs of pure Cu by applying the $< 1\overline{10} > \{111\}$ and $< 11\overline{2} > \{111\}$ shear strain and found an interesting variation tendency. In addition, Szajewski et al. [120] studied the core properties for Cu under a shear stress, and found that at higher shear stresses, the cores of each partial dislocation begin to overlap, and the two partial dislocations begin to recede. Liu et al. [121] found that the Peierls stress may exhibit quasi-periodically decreasing oscillations with increasing Escaig stress by using an improved SVPN model. All these unique findings suggest the necessary to investigate strain effects besides the widely studied solute effects on strengthening.

Although the strain effect may provide a unique solution to strengthening alone, it cannot replace solute strengthening. The widely studied solute strengthening or the "chemical" misfit induced by solute element still has many distinct characteristics. As shown in Fig. 9, for both Zn and Mg, the solute elements change the charge distribution and influence the charge transfer strongly around the faulted area, effects we find cannot be attained by strain modification. Under some conditions, a larger SFE modification range can be attained by solute strengthening than by straining. For instance, as shown in Fig. 6c, for pure Zn, both longitudinal tension and compression strain lead to a decreased γ_b . However, by solute modification, a much higher γ_{l_2} can be attained by introducing the solute element Cu, as shown in Fig. 3. Last, we note that in the application of biodegradable Zn-based and Mg-based alloys, solute elements not only improve the mechanical properties, but also modify the corrosion properties [6,13], whereas strain has been shown to detrimentally decrease the corrosion resistance [122].

5. Conclusions

In this work, we have investigated the synergetic effects of biocompatible solutes and strain on stacking fault energies, dislocation core structures and Peierls stress in biodegradable Zn-based and Mg-based alloys via an *ab initio*-informed Peierls-Nabarro model. The main results are as follows:

- (1) For all solute elements, the stronger solute effect is found in the Zn-based alloys than Mg-based alloys.
- (2) Considering in calculation, biocompatible solute elements Mg(Zn), Fe, Cu, Li, Al, Mn, we found that the solute Li has opposing solute effects on the intrinsic stacking fault energies on Mg and Zn.

- (3) Fe decreases SFEs and the increasing dislocation dissociation and Peierls stress because of the distinct charge polarization and the localized strain near the solute.
- (4) A much stronger strain induced strengthening or softening is found in the Zn-based alloys as compared to the Mg-based alloys. Although the SFEs, dislocation structures and Peierls stresses exhibit a similar trend in response to hydrostatic pressure, their response to longitudinal strain is substantially different. Analysis of the electronic and atomic structure changes attributes their differing response to the greater sensitivity of Zn to changes in the *c*/*a* ratio and chemical bonding strength.
- (5) The electronic structure analysis reveals that the electronic polarization at the hollow sites of hexagonal close packed structure and charge transfer between the solute and Zn (Mg) is responsible for the variations of SFEs, dislocation core structures and Peierls stresses. A pronounced charge polarization is found in both Zn₄₇Fe and Mg₄₇Fe, which might explain the fact that they respond little under strain conditions. When Fe is added, the chemical misfit dominates, and the influences of strain are comparatively less.

In conclusion, the synergetic effects of alloying and straining revealed here cannot be replaced by each effect alone. The space of possible alloying elements, combinations, and concentrations is vast, as well as the additional levels and modes of straining that could be considered in tandem. The work here introduces a framework in which to probe more combinations and opens alternative way to solve the tradeoff between strength and ductility, which is beyond the normal design rules purely based on either solute strengthening or strain effects alone.

Acknowledgments

This work is supported by the National Key Research and Development Program of China (No. 2016YFC1102500), National Natural Science Foundation of China (NSFC) (No. 51672015), National Thousand Young Talents Program of China, the Fundamental Research Funds for the Central Universities, and the Large Infrastructures for Research, Experimental Development and Innovations project "IT4Innovations National Supercomputing Center – LM2015070" and by the grant No. 17-27790S of the Grant Agency of the Czech Republic. I.J.B. acknowledges financial support from the National Science Foundation Designing Materials to Revolutionize and Engineer our Future (DMREF) program (NSF CMMI-1729887). SLS and ZKL would like to acknowledge the support from U.S. Department of Energy with the award No. DE-FE0031553.

Supplementary materials

Supplementary material associated with this article can be found, in the online version, at doi:10.1016/j.actamat.2019.09.059.

References

- [1] J.R. Davis, Handbook of Materials for Medical Devices, ASM International, 2003.
- [2] P.K. Bowen, E.R. Shearier, S. Zhao, R.J. Guillory, F. Zhao, J. Goldman, J.W. Drelich, Biodegradable metals for cardiovascular stents: from clinical concerns to recent Zn-allovs. Adv. Healthc. Mater. 5 (10) (2016) 1121–1140.
- [3] R. Hänsch, R.R. Mendel, Physiological functions of mineral micronutrients (Cu, Zn, Mn, Fe, Ni, Mo, B, Cl), Curr. Opin. Plant Biol. 12 (3) (2009) 259–266.
- [4] H. Tapiero, K.D. Tew, Trace elements in human physiology and pathology: zinc and metallothioneins, Biomed. Pharmacother. 57 (9) (2003) 399-411.
- [5] H.F. Li, Y.F. Zheng, L. Qin, Progress of biodegradable metals, Prog. Nat. Sci. 24 (5) (2014) 414–422.
- [6] E. Mostaed, M. Sikora-Jasinska, J.W. Drelich, M. Vedani, Zinc-based alloys for degradable vascular stent applications, Acta Biomater. 71 (2018) 1–23.
- [7] K. Törne, A. Örnberg, J. Weissenrieder, Influence of strain on the corrosion of magnesium alloys and zinc in physiological environments, Acta Biomater. 48 (2017) 541–550.

- [8] Q.Z. Chen, G.A. Thouas, Metallic implant biomaterials, Mater. Sci. Eng. R 87 (2015) 1–57.
- [9] M. Moravej, D. Mantovani, Biodegradable metals for cardiovascular stent application: interests and new opportunities, Int. J. Mol. Sci. 12 (7) (2011) 4250–4270
- [10] Z. Sheikh, S. Najeeb, Z. Khurshid, V. Verma, H. Rashid, M. Glogauer, Biodegradable materials for bone repair and tissue engineering applications, Materials 8 (9) (2015) 5744–5794.
- [11] M.P. Staiger, A.M. Pietak, J. Huadmai, G. Dias, Magnesium and its alloys as orthopedic biomaterials: a review. Biomaterials 27 (9) (2006) 1728–1734.
- [12] G.U. Xue-Nan, Y.F. Zheng, A review on magnesium alloys as biodegradable materials, Front. Mater. Sci. 4 (2) (2010) 111–115.
- [13] D. Vojtěch, J. Kubásek, J. Šerák, P. Novák, Mechanical and corrosion properties of newly developed biodegradable Zn-based alloys for bone fixation, Acta Biomater. 7 (9) (2011) 3515–3522.
- [14] P.K. Bowen, J. Drelich, J. Goldman, Zinc exhibits ideal physiological corrosion behavior for bioabsorbable stents, Adv. Mater. 25 (18) (2013) 2577–2582.
- [15] Y. Qi, H. Qi, Y. He, W. Lin, P.Z. Li, L. Qin, Y. Hu, L. Chen, Q. Liu, H. Sun, Strategy of metal-polymer composite stent to accelerate biodegradation of iron-based biomaterials, ACS Appl. Mater. Interfaces 10 (1) (2017) 182.
- [16] O.I. Velikokhatnyi, P.N. Kumta, First principles study of the elastic properties of magnesium and iron based bio-resorbable alloys, Mater. Sci. Eng. B 230 (2018) 20–23.
- [17] H. Hermawan, D. Dubé, D. Mantovani, Degradable metallic biomaterials: design and development of Fe–Mn alloys for stents, J. Biomed. Mater. Res. Part A 93A (1) (2010) 1–11.
- [18] M.G. Jiang, H. Yan, R.S. Chen, Enhanced mechanical properties due to grain refinement and texture modification in an AZ61 Mg alloy processed by small strain impact forging, Mater. Sci. Eng. A 621 (2015) 204–211.
- [19] M.G. Jiang, C. Xu, T. Nakata, H. Yan, R.S. Chen, S. Kamado, Development of dilute Mg-Zn-Ca-Mn alloy with high performance via extrusion, J. Alloys Compd. 668 (2016) 13-21.
- [20] S.L. Shang, W.Y. Wang, B.C. Zhou, Y. Wang, K.A. Darling, L.J. Kecskes, S.N. Mathaudhu, Z.K. Liu, Generalized stacking fault energy, ideal strength and twinnability of dilute Mg-based alloys: a first-principles study of shear deformation, Acta Mater. 67 (2014) 168–180.
- [21] D. Buey, L.G. Hector, M. Ghazisaeidi, Core structure and solute strengthening of second-order pyramidal <c+a> dislocations in Mg-Y alloys, Acta Mater. 147 (2018) 1–9.
- [22] B.L. Yin, Z.X. Wu, W.A. Curtin, First-principles calculations of stacking fault energies in Mg-Y, Mg-Al and Mg-Zn alloys and implications for activity <c+a> activity, Acta Mater. 136 (2017) 249–261.
- [23] H.F. Li, H.T. Yang, Y.F. Zheng, F.Y. Zhou, K.J. Qiu, X. Wang, Design and characterizations of novel biodegradable ternary Zn-based alloys with IIA nutrient alloying elements Mg, Ca and Sr, Mater. Des. 83 (2015) 95–102.
- [24] Z.B. Tang, H. Huang, J.I. Niu, L. Zhang, H. Zhang, J. Pei, J.Y. Tan, G.Y. Yuan, Design and characterizations of novel biodegradable Zn-Cu-Mg alloys for potential biodegradable implants, Mater. Des. 117 (2017) 84–94.
- [25] H.F. Li, X.H. Xie, Y.F. Zheng, Y. Cong, F.Y. Zhou, K.J. Qiu, X. Wang, S.H. Chen, L. Huang, L. Tian, Development of biodegradable Zn-1X binary alloys with nutrient alloying elements Mg, Ca and Sr, Sci. Rep. 5 (2015) 10719.
- [26] X.W. Liu, J.K. Sun, K.J. Qiu, Y.H. Yang, Z.J. Pu, L. Li, Y.F. Zheng, Effects of alloying elements (Ca and Sr) on microstructure, mechanical property and in vitro corrosion behavior of biodegradable Zn–1.5 mg alloy, J. Alloys Compd. 664 (2016) 444–452.
- [27] H.R. Bakhsheshi-Rad, E. Hamzah, H.T. Low, M. Kasiri-Asgarani, S. Farahany, E. Akbari, M.H. Cho, Fabrication of biodegradable Zn-Al-Mg alloy: mechanical properties, corrosion behavior, cytotoxicity and antibacterial activities, Mater. Sci. Eng. C 73 (2017) 215–219.
- [28] H.B. Gong, K. Wang, R. Strich, J.G. Zhou, In vitro biodegradation behavior, mechanical properties, and cytotoxicity of biodegradable Zn-Mg alloy, J. Biomed. Mater. Res. Part B 103 (8) (2015) 1632–1640.
- [29] J. Kubásek, D. Vojtěch, E. Jablonská, I. Pospíšilová, J. Lipov, T. Ruml, Structure, mechanical characteristics and in vitro degradation, cytotoxicity, genotoxicity and mutagenicity of novel biodegradable Zn-Mg alloys, Mater. Sci. Eng. C 58 (2016) 24–35.
- [30] S. Zhao, J.M. Seitz, R. Eifler, H.J. Maier, R.J. Guillory, E.J. Earley, A. Drelich, J. Goldman, J.W. Drelich, Zn-Li alloy after extrusion and drawing: structural, mechanical characterization, and biodegradation in abdominal aorta of rat, Mater. Sci. Eng. C 76 (2017) 301–312.
- [31] X.W. Liu, J.K. Sun, Y.H. Yang, F.Y. Zhou, Z.J. Pu, L. Li, Y.F. Zheng, Microstructure, mechanical properties, in vitro degradation behavior and hemocompatibility of novel Zn-Mg-Sr alloys as biodegradable metals, Mater. Lett. 162 (2016) 242–245.
- [32] J.L. Niu, Z.B. Tang, H. Huang, J. Pei, H. Zhang, G.Y. Yuan, W.J. Ding, Research on a Zn-Cu alloy as a biodegradable material for potential vascular stents application, Mater. Sci. Eng. C 69 (2016) 407–413.
- [33] Y.Q. Chen, W.T. Zhang, M.F. Maitz, M.Y. Chen, H. Zhang, J.L. Mao, Y.C. Zhao, N. Huang, G.J. Wan, Comparative corrosion behavior of Zn with Fe and Mg in the course of immersion degradation in phosphate buffered saline, Corros. Sci. 111 (2016) 541–555.
- [34] N.S. Murni, M.S. Dambatta, S.K. Yeap, G.R.A. Froemming, H. Hermawan, Cytotoxicity evaluation of biodegradable Zn-3Mg alloy toward normal human osteoblast cells, Mater. Sci. Eng. C 49 (2015) 560-566.

- [35] C. Wang, Z.T. Yu, Y.J. Cui, Y.F. Zhang, S. Yu, G.Q. Qu, H.b. Gong, Processing of a novel Zn alloy micro-tube for biodegradable vascular stent application, J. Mater. Sci. Technol. 32 (9) (2016) 925–929.
- [36] J. Kubasek, I. Pospisilova, D. Vojtech, E. Jablonska, T. Ruml, Structural, mechanical and cytotoxicity characterization of as-cast biodegradable Zn-xMg (x= 0.8-8.3%) alloys, Mater. Tehnol. 48 (5) (2014) 623-629.
- [37] D. Vojtech, J. Kubasek, J. Capek, I. Pospisilova, Comparative mechanical and corrosion studies on magnesium, zinc and iron alloys as biodegradable metals, Mater. Tehnol. 49 (6) (2015) 877–882.
- [38] E. Mostaed, M. Sikora-Jasinska, A. Mostaed, S. Loffredo, A.G. Demir, B. Previtali, D. Mantovani, R. Beanland, M. Vedani, Novel Zn-based alloys for biodegradable stent applications: design, development and in vitro degradation, J. Mech. Behav. Biomed. Mater. 60 (2016) 581–602.
- [39] Z.B. Tang, J.L. Niu, H. Huang, H. Zhang, J. Pei, J.M. Ou, G.Y. Yuan, Potential biodegradable Zn-Cu binary alloys developed for cardiovascular implant applications, J. Mech. Behav. Biomed. Mater. 72 (2017) 182–191.
- [40] H.R. Bakhsheshi-Rad, E. Hamzah, H.T. Low, M.H. Cho, M. Kasiri-Asgarani, S. Farahany, A. Mostafa, M. Medraj, Thermal characteristics, mechanical properties, in vitro degradation and cytotoxicity of novel biodegradable Zn-Al-Mg and Zn-Al-Mg-XBi alloys, Acta Metall. Sin. – Engl. Lett. 30 (3) (2017) 201–211.
- [41] S.H. Im, Y. Jung, S.H. Kim, Current status and future direction of biodegradable metallic and polymeric vascular scaffolds for next-generation stents, Acta Biomater. 60 (2017) 3–22.
- [42] L. Huang, C. Pu, R.K. Fisher, D.J.H. Mountain, Y. Gao, P.K. Liaw, W. Zhang, W. He, A Zr-based bulk metallic glass for future stent applications: materials properties, finite element modeling, and in vitro human vascular cell response, Acta Biomater. 25 (2015) 356–368.
- [43] Y. Yuan, A. Ma, X. Gou, J. Jiang, F. Lu, D. Song, Y. Zhu, Superior mechanical properties of ZK60 mg alloy processed by equal channel angular pressing and rolling, Mater. Sci. Eng. A 630 (2015) 45–50.
- [44] C. Xu, M. Zheng, S. Xu, K. Wu, E. Wang, G. Fan, S. Kamado, Improving strength and ductility of Mg-Gd-Y-Zn-Zr alloy simultaneously via extrusion, hot rolling and ageing, Mater. Sci. Eng. A 643 (2015) 137-141.
- [45] E. Mostaed, A. Fabrizi, D. Dellasega, F. Bonollo, M. Vedani, Microstructure, mechanical behavior and low temperature superplasticity of ecap processed ZM21 Mg alloy, J. Alloys Compd. 638 (2015) 267–276.
- [46] S.H. Zhang, I.J. Beyerlein, D. Legut, Z.H. Fu, Z. Zhang, S.L. Shang, Z.K. Liu, T.C. Germann, R.F. Zhang, First-principles investigation of strain effects on the stacking fault energies, dislocation core structure, and Peierls stress of magnesium and its alloys, Phys. Rev. B 95 (22) (2017) 224106.
- [47] G.S. Liu, J. Wang, Y. Shen, Density functional theory study of twin boundaries of zn under high pressure, Comput. Mater. Sci. 151 (2018) 106–116.
- [48] F. Kang, J.Q. Liu, J.T. Wang, X. Zhao, The effect of hydrostatic pressure on the activation of non-basal slip in a magnesium alloy, Scr. Mater. 61 (8) (2009) 844–847.
- [49] H. Li, Q.Q. Duan, X.W. Li, Z.F. Zhang, Compressive and fatigue damage behavior of commercially pure zinc, Mater. Sci. Eng. A 466 (1) (2007) 38–46.
- [50] G. Kresse, J. Furthmüller, Efficient iterative schemes for ab initio total-energy calculations using a plane-wave basis set, Phys. Rev. B 54 (16) (1996) 11169.
- [51] G. Kresse, D. Joubert, From ultrasoft pseudopotentials to the projector augmented-wave method, Phys. Rev. B 59 (3) (1999) 1758.
- [52] J.P. Perdew, K. Burke, M. Ernzerhof, Generalized gradient approximation made simple, Phys. Rev. Lett. 77 (18) (1996) 3865.
- [53] M. Methfessel, A.T. Paxton, High-precision sampling for brillouin-zone integration in metals, Phys. Rev. B 40 (6) (1989) 3616.
- [54] J. Nuss, U. Wedig, A. Kirfel, M. Jansen, The structural anomaly of zinc: evolution of lattice constants and parameters of thermal motion in the temperature range of 40 to 500K, Z. Anorg. Allg. Chem. 636 (2) (2010) 309–313.
- [55] U. Wedig, H. Nuss, J. Nuss, M. Jansen, D. Andrae, B. Paulus, A. Kirfel, W. Weyrich, Electronic origin of the structural anomalies of zinc and cadmium, Z. Anorg. Allg. Chem. 639 (11) (2013) 2036–2046.
- [56] Q.M. Hu, R. Yang, Basal-plane stacking fault energy of hexagonal close-packed metals based on the ising model, Acta Mater 61 (4) (2013) 1136–1145.
- [57] X.Z. Wu, R. Wang, S.F. Wang, Generalized-stacking-fault energy and surface properties for HCP metals: a first-principles study, Appl. Surf. Sci. 256 (11) (2010) 3409–3412.
- [58] F.W. Von Batchelder, R.F. Raeuchle, Lattice constants and brillouin zone overlap in dilute magnesium alloys, Phys. Rev. 105 (1) (1957) 59.
- [59] G.L. Clendenen, H.G. Drickamer, Effect of pressure on the volume and lattice parameters of magnesium, Phys. Rev. 135 (6A) (1964) A1643.
- [60] Z.R. Pei, D.C. Ma, M. Friák, B. Svendsen, D. Raabe, J. Neugebauer, From generalized stacking fault energies to dislocation properties: five-energy-point approach and solid solution effects in magnesium, Phys. Rev. B 92 (6) (2015) 064107.
- [61] G.A. Alers, J.R. Neighbours, The elastic constants of zinc between 4.2 and 670K, J. Phys. Chem. Solids 7 (1) (1958) 58–64.
- [62] G. Simmons, H. Wang, Single Crystal Elastic Constants and Calculated Aggregate Properties, The M.I.T. Press, Cambridge, 1971.
- [63] M. De Jong, I. Winter, D.C. Chrzan, M. Asta, Ideal strength and ductility in metals from second-and third-order elastic constants, Phys. Rev. B 96 (1) (2017) 014105.
- [64] A.R. Wazzan, L.B. Robinson, Elastic constants of magnesium-lithium alloys, Phys. Rev. 155 (3) (1967) 586.

- [65] C. Wang, H.Y. Wang, T.L. Huang, X.N. Xue, F. Qiu, Q.C. Jiang, Generalized-stack-ing-fault energy and twin-boundary energy of hexagonal close-packed au: a first-principles calculation, Sci. Rep. 5 (2015) 10213.
- [66] V. Vitek, Atomic structure of dislocations in intermetallics with close packed structures: a comparative study, Intermetallics 6 (7–8) (1998) 579–585.
- [67] H. Suzuki, Segregation of solute atoms to stacking faults, J. Phys. Soc. Jpn. 17 (2) (1962) 322–325.
- [68] J. Chen, J. Wei, H. Yan, B. Su, X. Pan, Effects of cooling rate and pressure on microstructure and mechanical properties of sub-rapidly solidified Mg-Zn-Sn-Al-Ca alloy. Mater. Des. 45 (2013) 300-307.
- [69] M. Jahnátek, J. Hafner, M. Krajčí, Shear deformation, ideal strength, and stacking fault formation of fcc metals: a density-functional study of Al and Cu, Phys. Rev. B 79 (22) (2009) 224103.
- [70] P.S. Branicio, J.Y. Zhang, D.J. Srolovitz, Effect of strain on the stacking fault energy of copper: a first-principles study, Phys. Rev. B 88 (6) (2013) 064104.
- [71] A. Kumar, B.M. Morrow, R.J. McCabe, I.J. Beyerlein, An atomic-scale modeling and experimental study of <c+a> dislocations in Mg, Mater. Sci. Eng. A 695 (2017) 270–278.
- [72] J.A. Yasi, T. Nogaret, D.R. Trinkle, Y. Qi, L.G. Hector Jr, W.A. Curtin, Basal and prism dislocation cores in magnesium: comparison of first-principles and embedded-atom-potential methods predictions, Model. Simul. Mater. Sci. Eng. 17 (5) (2009) 055012.
- [73] M. Ghazisaeidi, L.G. Hector, W.A. Curtin, First-principles core structures of <c+a> edge and screw dislocations in Mg, Scr. Mater. 75 (2014) 42–45.
- [74] C. Woodward, D.R. Trinkle, L.G. Hector Jr, D.L. Olmsted, Prediction of dislocation cores in aluminum from density functional theory, Phys. Rev. Lett. 100 (4) (2008) 045507.
- [75] S.K. Yadav, R. Ramprasad, A. Misra, X.Y. Liu, Core structure and Peierls stress of edge and screw dislocations in tin: a density functional theory study, Acta Mater. 74 (2014) 268–277.
- [76] E. Clouet, Screw dislocation in zirconium: an ab initio study, Phys. Rev. B 86 (14) (2012) 144104.
- [77] V.V. Bulatov, E. Kaxiras, Semidiscrete variational Peierls framework for dislocation core properties, Phys. Rev. Lett. 78 (22) (1997) 4221.
- [78] G. Lu, The Peierls-Nabarro model of dislocations: a venerable theory and its current development, in: Handbook of Materials Modeling, Springer, Dordrecht, 2005, pp. 793–811.
- [79] G. Schoeck, The generalized Peierls-Nabarro model, Philos. Mag. A 69 (6) (1994) 1085–1095.
- [80] V. Bulatov, W. Cai, Computer Simulations of Dislocations, Oxford University Press, Oxford, UK, 2006.
- [81] R.F. Zhang, S.H. Zhang, Y.Q. Guo, Z.H. Fu, D. Legut, T.C. Germann, S. Veprek, First-Principles design of strong solids: Approaches and applications, Physics Reports (2019), doi:10.1016/j.physrep.2019.09.004.
- [82] J. Kennedy, Particle swarm optimization, in: Encyclopedia of Machine Learning, Springer, 2011, pp. 760–766.
- [83] G. Schoeck, The core structure, recombination energy and Peierls energy for dislocations in Al, Philos. Mag. A 81 (5) (2001) 1161–1176.
- [84] B. Joos, M.S. Duesbery, The Peierls stress of dislocations: an analytic formula, Phys. Rev. Lett. 78 (2) (1997) 266.
- [85] P. Cordier, J. Amodeo, P. Carrez, Modelling the rheology of mgo under Earth's mantle pressure, temperature and strain rates, Nature 481 (7380) (2012) 177–180.
- [86] Y. Kamimura, K. Edagawa, A.M. Iskandarov, M. Osawa, Y. Umeno, S. Takeuchi, Peierls stresses estimated via the Peierls-Nabarro model using ab-initio γ-surface and their comparison with experiments, Acta Mater. 148 (2018) 255-262.
- [87] G. Lu, N. Kioussis, V.V. Bulatov, E. Kaxiras, Generalized-stacking-fault energy surface and dislocation properties of aluminum, Phys. Rev. B 62 (5) (2000) 3099–3108.
- [88] G. Liu, X. Cheng, J. Wang, K. Chen, Y. Shen, Peierls stress in face-centered-cubic metals predicted from an improved semi-discrete variation Peierls-Nabarro model, Scr. Mater. 120 (2016) 94–97.
- [89] G. Liu, X. Cheng, J. Wang, K. Chen, Y. Shen, Atomically informed nonlocal semi-discrete variational Peierls-Nabarro model for planar core dislocations, Sci. Rep. 7 (2017) 43785.
- [90] O.N. Mryasov, Y.N. Gornostyrev, M. van Schilfgaarde, A.J. Freeman, Complex evolution of dislocation core structure in a process of motion: model analysis with ab-initio parameterization, Mater. Sci. Eng. A 309-310 (2001) 138– 141
- [91] Y. Shen, X. Cheng, Dislocation movement over the Peierls barrier in the semi-discrete variational Peierls framework, Scr. Mater. 61 (5) (2009) 457–460.
- [92] Q. Zhang, T.W. Fan, L. Fu, B.Y. Tang, L.M. Peng, W.J. Ding, Ab-initio study of the effect of rare-earth elements on the stacking faults of Mg solid solutions, Intermetallics 29 (2012) 21–26.
- [93] J.E. Harris, B.C. Masters, The stacking fault energy of zinc and magnesium, Phys. Status Solidi B 9 (3) (1965) K181–K184.
- [94] R.L. Fleischer, Stacking fault energies of HCP metals, Scripta Metall 20 (2) (1986) 223–224.

- [95] Z. Wu, M.F. Francis, W.A. Curtin, Magnesium interatomic potential for simulating plasticity and fracture phenomena, Modell. Simul. Mater. Sci. Eng. 23 (1) (2015) 015004.
- [96] D. Hull, D.J. Bacon, Introduction to Dislocations, 5th ed., Butterworth-Heinemann, Oxford, 2011
- [97] W.B. Hutchinson, M.R. Barnett, Effective values of critical resolved shear stress for slip in polycrystalline magnesium and other hcp metals, Scr. Mater. 63 (7) (2010) 737–740.
- [98] T. Tsuru, D.C. Chrzan, Effect of solute atoms on dislocation motion in Mg: an electronic structure perspective, Sci. Rep. 5 (2015) 8793.
 [99] G.P.M. Leyson, W.A. Curtin, L.G. Hector Jr, C.F. Woodward, Quantitative pre-
- [99] G.P.M. Leyson, W.A. Curtin, L.G. Hector Jr, C.F. Woodward, Quantitative prediction of solute strengthening in aluminium alloys, Nat. Mater. 9 (9) (2010) 750–755.
- [100] G.P.M. Leyson, L.G. Hector, W.A. Curtin, Solute strengthening from first principles and application to aluminum alloys, Acta Mater. 60 (9) (2012) 3873–3884.
- [101] G.P.M. Leyson, L.G. Hector, W.A. Curtin, First-principles prediction of yield stress for basal slip in Mg-Al alloys, Acta Mater. 60 (13–14) (2012) 5197–5203.
- [102] R. Salloom, R. Banerjee, S.G. Srinivasan, Effect of β -stabilizer elements on stacking faults energies and ductility of α -titanium using first-principles calculations, J. Appl. Phys. 120 (17) (2016) 175105.
- [103] M.A. Khan, S. Yaqoob, Inhibitory effects of copper on bacterial and fungal growth, Int. J. Med. Res. Rev. 5 (05) (2017) 466–471.
- [104] A. Kafri, S. Ovadia, G. Yosafovich-Doitch, E. Aghion, In vivo performances of pure Zn and Zn-Fe alloy as biodegradable implants, J. Mater. Sci.: Mater. Med. 29 (7) (2018) 94.
- [105] J.Y. Zhang, P.S. Branicio, D.J. Srolovitz, Planar fault energies of copper at large strain: a density functional theory study, J. Appl. Phys. 116 (10) (2014) 103512.
- [106] G.N. Greaves, A.L. Greer, R.S. Lakes, T. Rouxel, Poisson's ratio and modern materials, Nat. Mater. 10 (11) (2011) 823.
- [107] E. Lilleodden, Microcompression study of Mg (0001) single crystal, Scr. Mater. 62 (8) (2010) 532–535.
- [108] C.M. Byer, B. Li, B. Cao, K.T. Ramesh, Microcompression of single-crystal magnesium, Scr. Mater. 62 (8) (2010) 536–539.
- [109] R.F. Zhang, Z.J. Lin, Y.S. Zhao, S. Veprek, Superhard materials with low elastic moduli: three-dimensional covalent bonding as the origin of superhardness in B6O, Phys. Rev. B 83 (9) (2011) 092101.
- [110] W.Y. Wang, S.L. Shang, Y. Wang, Z.G. Mei, K.A. Darling, L.J. Kecskes, S.N. Mathaudhu, X.D. Hui, Z.K. Liu, Effects of alloying elements on stacking fault energies and electronic structures of binary Mg alloys: a first-principles study, Mater. Res. Lett. 2 (1) (2014) 29–36.
- [111] J. Friedel, Les Dislocations, Gauthier-Villars, Paris, 1956.
- [112] R.L. Fleischer, Solution hardening, Acta Metall. 9 (1961) 996-1000.
- [113] R.L. Fleischer, Substitutional solution hardening, Acta Metall. 11 (1963) 203–209.
- [114] R. Labusch, A statistical theory of solid solution hardening, Phys. Status Solidi B 41 (2) (1970) 659–669.
- [115] R. Labusch, Statistische theorien der mischkristallhärtung, Acta Metall. 20 (7) (1972) 917–927.
- [116] J.A. Yasi, L.G. Hector Jr, D.R. Trinkle, First-principles data for solid-solution strengthening of magnesium: from geometry and chemistry to properties, Acta Mater. 58 (17) (2010) 5704–5713.
- [117] D.C. Ma, M. Friák, J.V. Pezold, D. Raabe, J. Neugebauer, Computationally efficient and quantitatively accurate multiscale simulation of solid-solution strengthening by ab initio calculation, Acta Mater. 85 (2015) 53–66.
- [118] Z.R. Liu, D.Y. Li, The electronic origin of strengthening and ductilizing magnesium by solid solutes, Acta Mater. 89 (2015) 225–233.
- [119] D.C. Ma, M. Friák, J. von Pezold, J. Neugebauer, D. Raabe, Ab initio study of compositional trends in solid solution strengthening in metals with low Peierls stresses, Acta Mater. 98 (2015) 367–376.
- [120] B.A. Szajewski, A. Hunter, I.J. Beyerlein, The core structure and recombination energy of a copper screw dislocation: a Peierls study, Philos. Mag. 97 (25) (2017) 2143–2163.
- [121] G. Liu, X. Cheng, J. Wang, K. Chen, Y. Shen, Quasi-periodic variation of Peierls stress of dislocations in face-centered-cubic metals, Int. J. Plast. 90 (2017) 156-166
- [122] E.M. Gutman, Mechanochemistry of Materials, Cambridge International Science Publishing, CambridgeUK, 1998.
- [123] B.L. Yin, Z.X. Wu, W.A. Curtin, Comprehensive first-principles study of stable stacking faults in hcp metals, Acta Mater. 123 (2017) 223–234.
- [124] J. Han, X.M. Su, Z.H. Jin, Y.T. Zhu, Basal-plane stacking-fault energies of Mg: a first-principles study of Li- and Al-alloying effects, Scr. Mater. 64 (8) (2011) 693-696.
- [125] M. Muzyk, Z. Pakiela, K.J. Kurzydlowski, Generalized stacking fault energy in magnesium alloys: density functional theory calculations, Scr. Mater. 66 (5) (2012) 219–222.
- [126] J.N. Wang, Prediction of Peierls stresses for different crystals, Mater. Sci. Eng. A 206 (2) (1996) 259–269.
- [127] Y. Kamimura, K. Edagawa, S. Takeuchi, Experimental evaluation of the Peierls stresses in a variety of crystals and their relation to the crystal structure, Acta Mater. 61 (1) (2013) 294–309.